

# The Shape, Multiplicity, and Evolution of Superclusters in $\Lambda$ CDM Cosmology

James J. Wray<sup>1</sup>

jwray@astro.princeton.edu

Neta Bahcall<sup>1</sup>

neta@astro.princeton.edu

Paul Bode<sup>1</sup>

bode@astro.princeton.edu

Carl Boettiger<sup>1</sup>

cboettig@princeton.edu

Philip F. Hopkins<sup>2</sup>

phopkins@cfa.harvard.edu

## ABSTRACT

We determine the shape, multiplicity, size, and radial structure of superclusters in the  $\Lambda$ CDM concordance cosmology from  $z = 0$  to  $z = 2$ . Superclusters are defined as clusters of clusters in our large-scale cosmological simulation. We find that superclusters are triaxial in shape; many have flattened since early times to become nearly two-dimensional structures at present, with a small fraction of filamentary systems. The size and multiplicity functions are presented at different redshifts. Supercluster sizes extend to scales of  $\sim 100 - 200h^{-1}$  Mpc. The supercluster multiplicity (richness) increases linearly with supercluster size. The density profile in superclusters is approximately isothermal ( $\sim R^{-2}$ ) and steepens on larger scales. These results can be used as a new test of the current cosmology when compared with upcoming observations of large-scale surveys.

*Subject headings:* large-scale structure of universe — cosmology: theory — galaxies: clusters: general

---

<sup>1</sup>Princeton University Observatory, Princeton, NJ 08544, USA

<sup>2</sup>Harvard-Smithsonian Center for Astrophysics, 60 Garden Street, Cambridge, MA 02138, USA

## 1. INTRODUCTION

Superclusters are the largest structures in the Universe. Their sizes span the range from a few times the radius of a typical galaxy cluster ( $\sim 3\text{-}4 h^{-1} \text{Mpc}$ ) to the lengths of the “Great Walls” of galaxies observed by the CfA Redshift Survey (Geller & Huchra 1989) and the Sloan Digital Sky Survey (Gott et al. 2003). These latter sizes of  $\sim 10^2 h^{-1} \text{Mpc}$  represent a significant fraction ( $\sim 10\%$ ) of the horizon scale.

Because they are so large relative to a typical survey volume, superclusters have proven difficult to study, especially in a statistical manner. Observationally, attempts to characterize the large-scale structure using distributions of galaxies date back to Hubble (1936), but these methods did not become powerful until the advent of galaxy cluster and galaxy redshift surveys. Abell (1958) used the Palomar Sky Survey to construct a catalog of rich clusters, with which he was able to find evidence for what he called “second-order clusters,” i.e. clusters of clusters, which are indeed superclusters. Subsequent work included Gregory & Thompson (1978)’s study of the supercluster containing the rich Coma cluster, and Gregory, Thompson, & Tifft (1981)’s work on the Perseus supercluster. Other observational approaches to supercluster identification have been based, like that of Abell (1958), on cluster catalogs (e.g. Oort 1983; Bahcall & Soneira 1984; Bahcall 1988; Einasto et al. 1994; Kolokotronis, Basilakos, & Plionis 2002) or on analysis of smoothed density fields (Einasto et al. 2003a,b). These have been important in characterizing the low-redshift Universe, but they have not yet allowed the study of supercluster evolution from early cosmic times (i.e., from redshifts of order unity). How do superclusters form, and how do their shapes, multiplicities, sizes, and structures evolve with time? The answers to these fundamental questions are not yet known.

Recently, there has been exciting progress on both the observational and computational fronts. The Sloan Digital Sky Survey (SDSS, York et al. 2000; Stoughton et al. 2002) is collecting deep, broadband imaging and spectroscopy of a large, contiguous portion of the sky. SDSS has created the largest galaxy redshift survey catalog to date, and much work is also underway to improve photometric redshift techniques (e.g. Csabai et al. 2000; Budavári et al. 2000), which would permit measurements of 3-D galaxy positions for the much larger SDSS imaging catalog. On the theoretical side, a concordance cosmological model has gained widespread acceptance (Bahcall et al. 1999; Bennett et al. 2003; Spergel et al. 2003). Applying this model to cosmological dynamics codes such as that described below, we can now reliably predict the properties and evolution of superclusters. The time is therefore ideal for a computational analysis of large-scale structure using new, powerful simulations, the results of which can be compared with current and future observations. Such comparisons will provide a new test of the current cosmological model, as well as shed

light on structure formation and evolution.

We begin by describing, in §2, the process by which clusters and in turn superclusters were identified in the simulation output. We provide quantitative descriptions of the multiplicity and size distributions of the identified superclusters, ready for comparison with future observations, in §3 and §4. We examine the radial structure of our superclusters in §5. We explore the dimensionality of superclusters in §6. The evolution of the above properties with redshift is presented in §7. Results for superclusters selected from only higher-mass clusters are presented in §8. Our conclusions are summarized in §9.

## 2. SELECTION OF SUPERCLUSTERS

### 2.1. The Simulation

We use the efficient, parallel dark matter simulation code of Bode & Ostriker (2003). A large-scale, high-resolution simulation was evolved with a particle-mesh method to compute long-range gravitational forces, and a tree code to treat high-density regions. We use the cosmological parameters of the concordance model:  $\Omega_m = 0.27$ ,  $\Omega_\Lambda = 0.73$ ,  $H_0 = 70 \text{ km s}^{-1} \text{ Mpc}^{-1}$ ,  $n_s = 0.96$ , and  $\sigma_8 = 0.84$  (cf. Spergel et al. 2003). A total of  $1260^3$  particles, each assigned the mass  $1.264 \times 10^{11} h^{-1} \text{ M}_\odot$ , is evolved in a periodic box  $1500 h^{-1} \text{ Mpc}$  on a side, and positions are saved at the appropriate times in order to construct a light cone with vertex at one corner of the box. Clusters are then identified in two different, partially overlapping volumes: a “low-redshift” sphere of radius  $1500 h^{-1} \text{ Mpc}$ , corresponding to a maximum redshift of  $z \approx 0.57$ , and a “high-redshift cone,” which includes the low- $z$  sphere’s positive octant ( $x > 0, y > 0, z > 0$ ) and extends this octant out to  $z = 3$ , a distance of  $\sim 4600 h^{-1} \text{ Mpc}$ . A total of 1,442,616 clusters are found in the low- $z$  sphere, and 720,550 in the high- $z$  cone. Further details on this light cone simulation are given by Hopkins, Bahcall, & Bode (2005), hereafter HBB.

### 2.2. Cluster Selection

Clusters are identified in the simulation using the friends-of-friends (FOF) algorithm (see HBB; Davis et al. 1985). The FOF results depend on the chosen linking length  $L$ . A common parameterization uses the linkage parameter  $b \equiv L/r_{av}$ , where  $r_{av}$  is the mean interparticle separation. This is useful in applications where the mean density of objects, and in turn their mean separation, changes over time. Holding  $b$  constant imposes the same minimum overdensity for clusters at all redshifts. We use the value  $b = 0.2$  (see also HBB),

corresponding to an overdensity of  $\sim 180$  times the mean density. The center of each FOF cluster is taken to be the position of the most bound particle. The virial radius, defined as the radius enclosing the virial overdensity expected from spherical top-hat collapse, is found using this center. In this analysis, we consider only clusters with virial mass threshold (i.e., the total mass within the virial radius)  $M_{vir} \geq 1.75 \times 10^{13} h^{-1} M_{\odot}$ . This mass threshold is typical for a poor cluster of galaxies. The mean mass of all clusters in the low- $z$  sphere is  $\sim 4.40 \times 10^{13} h^{-1} M_{\odot}$ . In §8 we discuss superclusters selected from clusters with a higher mass threshold.

The ellipticities of the clusters identified at low and high  $z$  are studied in detail by HBB. Relevant to our present work on superclusters, they find alignments between nearby cluster pairs out to separations of  $\sim 100 h^{-1}$  Mpc; the strength of alignment increases with redshift and with decreasing cluster separation. HBB explain these alignments as being due to clusters forming and gathering material along “filamentary superstructures”; they provide evidence for overdensities along the separation vectors between pairs of aligned clusters.

### 2.3. Supercluster Selection

As demonstrated by Abell (1958), Bahcall (1988) and references therein, superclusters can be identified by their overdensity of clusters. We use the FOF method to identify superclusters from the cluster sample defined above (§2.1-2.2). The mean density of clusters in the low- $z$  sphere (we shall not discuss the high- $z$  cone until §7) is  $n_{av} = 1.02 \times 10^{-4} (h^{-1} \text{ Mpc})^{-3}$ , yielding a mean intercluster separation of  $r_{av} \equiv n_{av}^{-1/3} = 21.4 h^{-1} \text{ Mpc}$ . We therefore select linking lengths of  $L = 3, 5, 7$ , and  $10 h^{-1} \text{ Mpc}$ , corresponding to  $b \approx 0.14, 0.23, 0.33$ , and 0.47, respectively. All scales in this paper are in comoving coordinates. The different linking lengths sample different portions of the supercluster geometry. Small linking lengths identify only the dense cores of superclusters, whereas larger linking lengths allow the FOF algorithm to percolate to lower-density filaments of clusters. Large  $L$ -values therefore reach to the outer parts of superclusters, as well as identify looser superclusters, and often connect structures that appear discrete with smaller  $L$ .

We use Monte Carlo simulations to compare the significance of the selected superclusters with that of random associations. Clusters are placed at randomly chosen positions within a sphere such that the total number density is the same as that for the simulated clusters, and the FOF method is applied, as before, with  $L = 3, 5, 7$ , and  $10 h^{-1} \text{ Mpc}$ . We find significantly fewer clusters per supercluster, and significantly fewer superclusters down to multiplicity as small as 3, for all four linking lengths tested. This result implies that most of the superclusters are real, even for  $L = 10 h^{-1} \text{ Mpc}$ . The only exception is the case of binary

clusters (superclusters with only 2 members) selected with  $L = 10h^{-1}$  Mpc, of which we find only  $\sim 25\%$  more using the simulated clusters than we do with the Monte Carlo sample. The random rate of superclusters is typically  $< 10\%$  for  $N > 3$  superclusters, decreasing to  $< 1\%$  for  $N > 6$  superclusters. The Monte Carlo results are compared with the  $\Lambda$ CDM multiplicity functions below.

To help visualize the typical geometries of superclusters identified by the FOF method, we present supercluster maps of a typical region (a cube of side length  $200h^{-1}$  Mpc, concentric with the low- $z$  sphere) for  $L = 7h^{-1}$  Mpc (Figs. 1-2). Each point is a cluster, and a given symbol represents membership in the same supercluster. The maps present a projection of the 3-D distribution onto the  $xy$ -plane in the first plot, and onto the  $xz$ -plane in the second plot. Viewing the plots in turn corresponds to a  $90^\circ$  rotation of the viewing angle about the  $x$ -axis. For clarity, we show only superclusters with at least 5 member clusters. Members of a supercluster that extend outside the limits of our cubical region are not shown, so some superclusters appear to have fewer members than the imposed minimum. Similar maps generated with  $L = 5$  or  $10h^{-1}$  Mpc show, as expected, that neighboring superclusters are often connected into one when the linking length is increased. This is especially true when  $L$  increases to  $10h^{-1}$  Mpc, resulting in many large, complicated structures with central cores joining multiple lower-density filaments.

### 3. SUPERCLUSTER MULTIPLICITY FUNCTION

The *multiplicity* of a supercluster is the number of clusters it contains,  $N$ . In Fig. 3 we present, for various linking lengths, the integrated supercluster multiplicity function — the number density (per cubic comoving  $h^{-1}$  Mpc) of superclusters with  $N$  or more members, as a function of  $N$ .

Longer linking lengths yield more superclusters of all multiplicities, as expected. Shorter linking lengths yield curves that rise more steeply toward low multiplicities, implying that they preferentially find small superclusters with low multiplicity. Conversely, longer linking lengths find a higher percentage of larger, richer superclusters. The shorter linking lengths naturally trace high-density regions (e.g., dense cores of superclusters), while larger linking lengths characterize lower-density regions, such as the outer parts of superclusters or diffuse superclusters. Small  $L$  can also divide structures that are identified with larger linking lengths. The fact that we see superclusters with  $\sim 40$  or more clusters may seem surprising, but the total number density of such structures is only  $10^{-8}$  per  $(h^{-1}\text{ Mpc})^3$ , and it is based on a very low mass threshold of cluster members,  $M_{vir} \geq 1.75 \times 10^{13} h^{-1} \text{ M}_\odot$ . Such clusters are numerous, and any comparison with observations should of course account for this threshold.

For superclusters selected using higher-mass clusters, see §8.

#### 4. SUPERCLUSTER SIZE FUNCTION

The supercluster size function — i.e., the number of superclusters above a given size — is presented in Fig. 4 for different linking lengths. The size of a supercluster is defined as the maximum distance of any member cluster from the supercluster center of mass. As with the multiplicity function, the size function rises more steeply for shorter linking lengths. This implies that the longer linking lengths find a greater ratio of large superclusters to small superclusters, analogous to the result for the multiplicity function.

We find that the largest supercluster radii are  $\sim 80h^{-1}$  Mpc, corresponding to diameters of  $\sim 160h^{-1}$  Mpc. This is consistent with the largest structures seen in observations (e.g. Bahcall & Soneira 1984; Geller & Huchra 1989; Gott et al. 2003), and it is also the largest distance at which HBB detect cluster alignment in the simulation.

#### 5. RADIAL STRUCTURE

The average multiplicity of superclusters is plotted as a function of supercluster size for different linking lengths in Fig. 5. For  $N = 2$  or  $3$  — objects more aptly called binary or triple clusters than superclusters — the maximum radius is set mainly by the separation(s) of the 2 or 3 clusters; thus the average multiplicity changes slowly over this range of separations. Beyond this regime, the multiplicity and size of superclusters appear to be related nearly linearly. This result suggests that the spherically averaged density profile in superclusters is roughly *isothermal*; i.e.,  $n(r) \propto r^{-2}$ , where the cluster number density  $n(r)$  satisfies:

$$N = \int_0^{R_{max}} n(r) 4\pi r^2 dr \quad (1)$$

This profile yields multiplicity  $N \propto R_{max}$  for  $n(r) \propto r^{-2}$ .

We can investigate the spherically averaged density profile more directly by examining the distribution of clusters within individual superclusters and determining the average number density profile for the entire sample. To do so, we superpose the centers-of-mass (calculated using only the mass in clusters) of all superclusters, and scale all superclusters to the same size by dividing all cluster coordinates (relative to the center-of-mass) for a given supercluster by its  $R_{max}$ . We add up the total number of clusters inside radial bins, divided by the total number of clusters in superclusters for the given linking length.

The results are plotted in Fig. 6. The points trace the integrated cluster number density fractions in the superclusters. We have included only superclusters with 5 or more members (the concept of a radial density profile loses meaning for groups of only a few clusters). Even with this filter, because the multiplicity function drops off rapidly, most of the superclusters used to make this plot have only 5 or 6 members. This fact affects the plot’s appearance in two ways. Firstly, only in few cases will one of the five members happen to lie very near the supercluster’s center-of-mass; thus it is only at  $R/R_{max} \gtrsim 0.2$  that we begin to find a significant fraction of the clusters. Secondly, one out of roughly five clusters in each supercluster lies at  $R/R_{max} = 1$ . Thus, for the smaller linking lengths, the integrated number fraction approaches a limit of  $\sim 0.8$ ; for the larger linking lengths, which find richer superclusters, the limiting fraction is slightly higher. By definition, the integrated fraction jumps to 1 at  $R = R_{max}$  for all linking lengths.

Over the range  $0.3 \lesssim R/R_{max} \lesssim 0.7$ , the best-fit power-law relation of the number density curves in Fig. 6 is linear (we omit the  $L = 3h^{-1}$  Mpc curve, which is noisy because of the small number of superclusters found with this linking length). This linear relationship indeed implies  $n(r) \sim r^{-2}$  for the supercluster density profile in this range. The profile steepens on larger scales.

The average mass of clusters in superclusters,  $M = 4.8 \times 10^{13}h^{-1} M_\odot$  for the  $L = 7h^{-1}$  Mpc superclusters, is somewhat larger than the average mass of clusters in the total sample,  $M = 4.4 \times 10^{13}h^{-1} M_\odot$ , indicating that superclusters contain slightly more massive clusters, on average, than the mean. The  $L = 7h^{-1}$  Mpc superclusters with  $N \geq 5$  members have an even higher average cluster mass of  $M = 5.5 \times 10^{13}h^{-1} M_\odot$ , implying that richer superclusters contain more massive clusters than poorer superclusters.

## 6. SUPERCLUSTER SHAPES

We measure the shape, and in particular the dimensionality, of a given supercluster by fitting a 3-D ellipsoid to the distribution of its member clusters. We use the code developed by HBB to fit ellipsoids to the dark matter particles comprising their clusters. The code constructs, for a given supercluster, the  $3 \times 3$  matrix of second moments of cluster positions relative to the supercluster center-of-mass, i.e.

$$I_{ij} = \sum x_i x_j m, \quad (2)$$

where  $x_i$  and  $x_j$  are two of the position coordinates for a given cluster, and  $m$  is the mass of the cluster; the sum is over all member clusters. The eigenvalues of this matrix are simply the three axis lengths of the best-fit ellipsoid for the supercluster, times a known

constant. We shall denote these lengths  $a_1, a_2, a_3$  for the primary, secondary, tertiary axes, respectively; i.e.,  $a_1 \geq a_2 \geq a_3$ . We restrict our analysis to superclusters with  $N \geq 5$ ; for poorer superclusters, the “best-fit ellipsoid” would not be very meaningful.

We have already examined size distributions for superclusters (§4), so we now focus on the *axis ratios*, which allow us to probe the shape and dimensionality of superclusters. Fig. 7 displays the distribution of *primary axis ratios*  $a_2/a_1$  for superclusters selected with  $L = 5, 7, 10h^{-1}$  Mpc. Fig. 8 shows the distribution of *secondary axis ratios*  $a_3/a_2$ . The mean and peak axis ratios from each curve in these two figures are listed in Table 1.

The secondary axis ratios are generally smaller than the primary axis ratios. We find that a primary axis ratio of  $a_2/a_1 \approx 0.6$  is typical for superclusters selected using a broad range of linking lengths; this corresponds to a primary ellipticity of  $\epsilon_1 \equiv 1 - a_2/a_1 \approx 0.4$ . The secondary axis ratio is more strongly dependent on the linking length used to find the superclusters. For  $L = 5h^{-1}$  Mpc, we find typical  $a_3/a_2$  of  $\sim 0.45$ , corresponding to a secondary ellipticity of  $\epsilon_2 \equiv 1 - a_3/a_2 \approx 0.55$ ; for  $L = 10h^{-1}$  Mpc, we more commonly find  $a_3/a_2 \approx 0.25$ , or  $\epsilon_2 \approx 0.75$ .

These measurements allow us to construct a picture of the typical shape and dimensionality of superclusters. The interpretation of different ellipticities can be described as follows:

1. A combination of low primary and high secondary ellipticity (i.e., high primary and low secondary axis ratio) is typical of two-dimensional pancake-like structures (two dimensions are large, and one is small).
2. A combination of high primary and low secondary ellipticity is typical of one-dimensional filamentary structures (one dimension is large, and two are small).
3. A combination of primary and secondary ellipticities that are both significantly greater than zero ( $\epsilon_{1,2} \gtrsim 0.3$ ) is typical of structures most appropriately described as triaxial (each dimension is a different size).
4. If both ellipticities are low, then the distribution is nearly spherical.

The results we find suggest that superclusters are typically triaxial structures nearing 2-D, pancake-like structures at  $z \approx 0$ . They are neither spherical nor purely filamentary in nature. As the linking length is increased, the resulting superclusters become more two-dimensional; the cores of superclusters are thus more triaxial, spreading out to more pancake-like structures on larger scales.

We plot bivariate distributions of  $a_2/a_1$  and  $a_3/a_2$  in Figs. 9-11 for  $L = 10, 7, 5h^{-1}$  Mpc, respectively. The  $L = 5h^{-1}$  Mpc plot uses larger bins to keep the distribution relatively smooth given the small number of  $N \geq 5$  superclusters. Applying the interpretation rules listed above, 1-D structures reside in the upper left corner of the distributions, 2-D in the lower right corner, and 3-D (spherical) in the upper right. Points in the middle or toward the lower left corner represent triaxial structures.

The majority of our superclusters are triaxial for all linking lengths. We can quantify this triaxiality using the measurement commonly employed for geometrical descriptions of elliptical galaxies, first introduced explicitly by Statler (1994):

$$T \equiv \frac{1 - (a_2/a_1)^2}{1 - (a_3/a_1)^2} \quad (3)$$

With  $a_1 \geq a_2 \geq a_3$ ,  $T$  will take on values between 0 and 1 (unless  $a_1 = a_2 = a_3$ , in which case  $T$  is undefined). Two-dimensional pancake structures approach  $T \rightarrow 0$ , while filaments approach  $T \rightarrow 1$  (note, however, that the increase is not linear with axis ratio). Intermediate values of  $T$  represent triaxial systems, with triaxiality increasing with  $T$ . By this measure our low- $z$  superclusters are triaxial, ranging from a mean of  $T \approx 0.65$  for  $L = 10h^{-1}$  Mpc to  $T \approx 0.69$  for  $L = 5h^{-1}$  Mpc.

Fig. 9 shows that a large majority of the superclusters identified using  $L = 10h^{-1}$  Mpc are more nearly two-dimensional than one-dimensional. No nearly spherical superclusters are found with this linking length, but there is a smaller population of filamentary structures. Figs. 10-11 show similar distributions, but with progressively fewer flattened structures for  $L = 7$  and  $5h^{-1}$  Mpc. This is the same trend depicted in Fig. 8 as a shift toward lower secondary axis ratio with increasing linking length. Figs. 10-11 also show significantly higher fractions of filamentary structures — i.e., superclusters with low primary axis ratio and a secondary axis ratio approaching one.

This trend suggests that most superclusters at  $z \approx 0$  are triaxial structures with one dimension considerably smaller than the other two. This geometry is apparent in Fig. 9, where a large FOF linking length is used. Since the superclusters are not completely flat, smaller linking lengths may probe only the dense core regions, which are smaller in size than the supercluster thickness. Thus, while the thickness sets an upper bound to the tertiary axis length identified with any linking length, the higher  $L$ -values find longer primary and secondary axes by probing farther out into the pancake. This causes larger linking lengths to find a smaller mean secondary axis ratio, and reveal the underlying 2-D nature of the large-scale superclusters. Similarly, for a given  $L$ , the largest, highest-multiplicity superclusters ( $N > 10$ ) are on average flatter ( $a_3/a_2 \approx 0.24$  for  $L = 10h^{-1}$  Mpc) than those with  $N = 5-10$  ( $a_3/a_2 \approx 0.35$ ).

For all linking lengths we see a tail in the distribution that describes structures which are very nearly one-dimensional. Thus, some mass concentrations are filamentary at  $z \approx 0$ , especially in the relatively dense regions probed by  $L = 5h^{-1}$  Mpc. Indeed, we would expect structures that have collapsed along two dimensions to be of higher average density than those that have collapsed along only one dimension. This result agrees with HBB’s identification of filamentary density enhancements in the large-scale structure; here we add the prediction of more diffuse flattened structures surrounding and possibly connecting the filaments.

## 7. SUPERCLUSTER EVOLUTION

We examine the time evolution of the supercluster properties studied above. We study superclusters in two redshift slices at  $0.8 \leq z \leq 1.2$  and  $1.7 \leq z \leq 2.4$ , denoted  $z \approx 1$  and  $z \approx 2$ , respectively.

Superclusters are identified by the FOF method as before. However, since the cluster abundance decreases at higher redshift, and their mean separation thus increases, we compare superclusters found at different redshifts *not* with the same linking length  $L$ , but instead with the same linkage parameter  $b \equiv L/r_{av}$ , where  $r_{av}$  is the mean comoving intercluster separation. As discussed in §2.2, this approach sets a minimum overdensity for detection of superclusters, which is constant with redshift.

This use of a constant linkage parameter accounts for the reduced density of clusters at high redshift. However, because clusters are clustered, the density of superclusters depends on the relative rates of cluster formation in regions of high density vs. low density. Hierarchical supercluster formation, in which clusters gravitate toward each other over time, also contributes to a reduced supercluster density at early times.

We indeed find a lower density of superclusters in the high- $z$  cone. The total number of superclusters decreases by a factor of a few from  $z \approx 0$  to  $z \approx 1$ , and by over an order of magnitude from  $z \approx 1$  to  $z \approx 2$ . In order to construct a sufficiently large sample, we consider broad ranges in redshift, especially for the  $z \approx 2$  slice. In addition, we omit the  $b$ -value corresponding to the  $L = 3h^{-1}$  Mpc ( $z \approx 0$ ) case from our subsequent analysis, as it results in too few superclusters at high redshift.

As stated in §2.3, our  $z \approx 0$  linking lengths of  $L = 5, 7, 10h^{-1}$  Mpc correspond to  $b = 0.23, 0.33, 0.47$ , respectively. We use these latter linkage parameters  $b$  to refer to the linking lengths used in our subsequent analysis. A given value of the  $b$ -parameter can be converted to an actual comoving linking length at a given redshift simply by multiplying by

the mean intercluster separation at that redshift. The mean cluster densities in our  $z \approx 1$  and  $z \approx 2$  shells are  $n_{av} = 3.53 \times 10^{-5}$  and  $2.57 \times 10^{-6} (h^{-1} \text{Mpc})^{-3}$ , corresponding to mean cluster separations of  $r_{av} = 30.5$  and  $73.0 h^{-1} \text{Mpc}$ , respectively. Therefore,  $b = 0.23, 0.33$ , and  $0.47$  correspond to  $L = 7, 10$ , and  $14.3 h^{-1} \text{Mpc}$  at  $z \approx 1$ , and  $16.8, 24$ , and  $34.3 h^{-1} \text{Mpc}$  at  $z \approx 2$ .

### 7.1. The Multiplicity Function

The evolution of the multiplicity function is presented in Fig. 12. We present the integrated multiplicity function for all three redshifts, using two different values of  $b$ . The number density of superclusters drops noticeably with increasing redshift. Monte Carlo simulations analogous to those described in §2.3 were also run at  $z \approx 1$  and  $2$ , with results similar to those obtained at low  $z$ : the multiplicity functions are physically significant for all multiplicities and linking lengths, except for binary clusters in the  $b = 0.47$  case, where only  $\sim 30\%$  more binary clusters are found over the Monte Carlo results.

The redshift evolution of the multiplicity function depends on the linking length of the superclusters. The vertical distances between the  $b = 0.47$  curves in Fig. 12 increase with increasing multiplicity, implying that the abundance of the richest (highest- $N$ ) superclusters found with this linking length drops off especially swiftly with increasing  $z$ . However, for  $b = 0.23$  the vertical distances *decrease* with increasing  $N$ , to the extent that the abundance of the richest superclusters found with this linking length is in fact roughly the same at  $z \approx 1$  as it is today. We interpret these trends as further evidence that small linking lengths (e.g.  $b = 0.23$ ) select the densest regions of superclusters. Whereas the larger linking lengths do not find many rich superclusters at high redshift because of the lack of clusters, the smaller linking lengths find the same dense supercluster cores even at much earlier times. These dense cores are likely the sites of the largest overdensities present at early times, and the first places where observable structures form through gravitational collapse. Thus smaller linking lengths relative to the mean intercluster separation are needed to locate the highest overdensities in the observable Universe. The lack of rich superclusters at high  $z$  is also evidence that these structures form largely through gravitational accretion of clusters that are initially too distant to be identified as supercluster members.

Supercluster size remains highly correlated with multiplicity at high  $z$ , but with a lower  $N - R_{max}$  normalization than at low  $z$ . The size function does not evolve significantly with redshift for the larger superclusters (see Fig. 13), while, as expected, the number of cluster members decreases.

## 7.2. Dimensionality

Using the method described in §6, we fit ellipsoids to the superclusters identified at  $z \approx 1$  and  $z \approx 2$ . Because we only perform these fits on superclusters with  $N \geq 5$ , which are rare at high redshift, the statistical uncertainties are larger. For example, only 68 superclusters are identified at  $z \approx 2$  for  $b = 0.23$ .

We use the axis ratios of the best-fit ellipsoids to characterize the evolution of supercluster dimensionality. Tables 2 and 3 present the mean primary and secondary axis ratios, respectively, for  $b = 0.23, 0.33, 0.47$  at  $z \approx 0, 1, 2$ . We also construct the axis ratio distributions (similar to Figs. 7-8) as a function of  $z$  for  $b = 0.33$  and  $0.47$  (Figs. 14-17); there are too few  $b = 0.23$  superclusters at high redshift to create meaningful distributions. The number of high-redshift superclusters is too low to construct bivariate distributions like Figs. 9-11 with reasonably high resolution, but we can consider how the changes in *mean* ratios correspond to translations of these distributions.

The strongest evolution observed is the increase in the secondary axis ratio with increasing redshift, for  $b = 0.47$  (Fig. 16). Most of the change occurs between  $z \approx 0$  and  $z \approx 1$ , with only a slight additional increase between  $z \approx 1$  and  $z \approx 2$  (see Table 3). Typical secondary axis ratios increase from  $a_3/a_2 \approx 0.25$  at low  $z$  to  $a_3/a_2 \approx 0.45$  at high  $z$ . Thus the flattened structures observed with  $b = 0.47$  at  $z \approx 0$  (see §6) appear less flattened at high redshifts, indicating their gravitational collapse over time. Fig. 17 indicates very little evolution in the secondary axis ratio for superclusters identified with  $b = 0.33$ , but the population of high-density filaments with  $a_3/a_2 \approx 1$  evolves between  $z \approx 1$  and  $z \approx 0$ , as there are almost none of these filamentary structures at high redshift.

The primary axis ratios are slightly smaller at higher redshifts for both  $b = 0.33$  and  $0.47$ . Typical values decrease from  $a_2/a_1 \approx 0.6$  at  $z \approx 0$  to  $a_2/a_1 \approx 0.5$  at  $z \approx 1-2$ . In a plot similar to Figs. 9-11, this would correspond to a leftward shift in the distribution, i.e. a shift toward greater triaxiality at high redshift, and a shift to a 2-D geometry as the systems approach  $z \approx 0$ . Quantitatively, our high- $z$  superclusters have mean triaxiality  $T \approx 0.79$  for both linking lengths, significantly higher than the mean  $T$  for any linking length at low  $z$ .

We conclude that superclusters had highly triaxial structure at early times, and that between a cosmological look-back time of  $\sim 8$  Gyr (corresponding to  $z \approx 1$  for the cosmology described in §2.1) and the present day, many collapsed along their smallest dimensions to form the more nearly pancake-like structures observed in the simulation at  $z \approx 0$ . In the same span of time, some structures in regions of highest density also collapsed along a second dimension to form nearly one-dimensional filaments.

## 8. SUPERCLUSTERS SELECTED USING HIGH-MASS CLUSTERS

How do the supercluster properties change if superclusters are selected using higher-mass clusters as their seeds? While the abundance of high-mass clusters is significantly lower, and the statistical uncertainties larger, the massive clusters are more easily detected in observational surveys. We repeat the analysis described above for superclusters selected using the rarer, higher-mass clusters with  $M_{vir} \geq 1 \times 10^{14}h^{-1} M_{\odot}$ . This threshold corresponds to typical “rich clusters” (e.g. Abell 1958; Bahcall 1988). There are  $9.68 \times 10^4$  clusters above this mass threshold at  $z \approx 0$ , and  $4.88 \times 10^3$  clusters at  $z \approx 1$ . The cluster abundance is  $6.8 \times 10^{-6}(h^{-1} \text{Mpc})^{-3}$  at  $z \approx 0$ , decreasing to  $0.8 \times 10^{-6}(h^{-1} \text{Mpc})^{-3}$  at  $z \approx 1$ . The intercluster mean separation is  $52.7h^{-1} \text{Mpc}$  at  $z \approx 0$ , increasing to  $107.9h^{-1} \text{Mpc}$  at  $z \approx 1$ .

Superclusters are selected from these clusters at  $z \approx 0$  and  $z \approx 1$  using the linkage parameters  $b = 0.33$  and  $0.47$ ; these correspond to  $L = 17.4$  and  $24.8h^{-1} \text{Mpc}$  respectively at  $z \approx 0$ , and  $L = 35.6$  and  $50.7h^{-1} \text{Mpc}$  at  $z \approx 1$ . The large linking lengths  $L$  reflect the large mean intercluster separation of these massive clusters. We also include, for comparison, the smaller linking length of  $L = 10h^{-1} \text{Mpc}$  at  $z \approx 0$ .

A map of the  $z \approx 0$  superclusters selected with  $b = 0.33$  is presented in Figs. 18-19; this can be compared with the similar map (Figs. 1-2) of superclusters selected with the low-mass clusters. As expected, fewer superclusters and a smaller number of cluster members are observed. The overall structure of the superclusters is not significantly changed, as described below.

The multiplicity function of the superclusters is presented in Fig. 20 for both  $z \approx 0$  and  $1$ . The results show, as expected, a similar shape to the multiplicity function of superclusters selected using the more numerous low-mass clusters (Figs. 3, 12, 13), but with a greatly reduced amplitude: the number of superclusters at a given multiplicity is lower, and—equivalently—the supercluster multiplicity (richness) is smaller for a given supercluster abundance. This is partly due to the much smaller number of massive clusters. The evolution of the multiplicity function is stronger than that of superclusters selected with low-mass clusters (cf. Fig. 12). Superclusters with linkage parameters of  $b \approx 0.2 - 0.33$  contain up to  $\sim 10 - 15$  rich clusters at  $z \approx 0$ . The supercluster multiplicity decreases sharply at higher redshifts.

The supercluster size function is presented in Fig. 21. The maximum size of  $z \approx 0$  superclusters ranges from  $\sim 40h^{-1} \text{Mpc}$  (i.e., twice the plotted  $R_{max}$  radius) for  $L = 10h^{-1} \text{Mpc}$ , to  $\sim 90h^{-1} \text{Mpc}$  for  $L = 17.4h^{-1} \text{Mpc}$  ( $b = 0.33$ ), to  $\sim 200h^{-1} \text{Mpc}$  for  $L = 24.8h^{-1} \text{Mpc}$  ( $b = 0.47$ ). For a given linkage parameter  $b$ , the maximum supercluster size is somewhat larger than that of superclusters selected with low-mass clusters, since the linking

length values  $L$  are larger. For a given value of  $b$ , no significant evolution is observed in the size of the largest superclusters, reflecting the existence of these extended structures at early times. The same result is observed for superclusters selected with the lower mass threshold clusters. The number of cluster members within these large structures decreases with redshift, as seen above, due to the lowered cluster abundance at high  $z$ .

The supercluster multiplicity versus size relation is presented in Fig. 22. This relation is similar—but reduced in amplitude, as expected—to the superclusters selected with the lower mass threshold clusters. A nearly linear relation between multiplicity and size is observed for all but the binary clusters.

The supercluster ellipticity distribution is presented in Figs. 23-24 for the primary and secondary axis ratios, respectively. The superclusters exhibit a triaxial geometry on average, but with significantly larger scatter than the more numerous superclusters selected with lower-mass clusters (Figs. 14-17). The mean primary and secondary axis ratios are each  $\sim 0.4$  to  $0.5$ ; these ratios do not change significantly with either linking length or with redshift to  $z \approx 1$ . The distribution of ellipticities around this mean is, however, quite broad. The supercluster shapes are not significantly different from those selected using the lower-mass clusters, except for the stronger flattening observed in the latter at  $z \approx 0$ , where the mean triaxial shape has evolved slightly towards a flattened two-dimensional shape (with  $a_2/a_1 \sim 0.6$  and  $a_3/a_2 \sim 0.3 - 0.4$ ). The superclusters selected with high-mass clusters are triaxial, with somewhat higher triaxiality at  $z \approx 0$  than those selected using lower-mass clusters—i.e., the high-mass superclusters are approaching a slightly more filamentary nature, with mean axis ratios of  $\sim 0.4$  in both  $a_2/a_1$  and  $a_3/a_2$  (cf. Figs. 9-11), and a mean triaxiality of  $T = 0.8 - 0.85$ .

## 9. CONCLUSIONS

We have investigated the multiplicities, sizes, radial structures, and dimensionalities of superclusters from  $z \approx 0$  to  $z \approx 2$  in  $\Lambda$ CDM cosmology. The results can be used as predictions for testing the cosmology with future observations, as well as for an improved understanding of structure formation.

At low redshift, we predict a total number density of  $\sim 4 \times 10^{-6}$ ,  $2 \times 10^{-6}$ , and  $3 \times 10^{-7}(h^{-1} \text{ Mpc})^{-3}$  superclusters with at least five member clusters with mass  $M_{vir} \geq 1.75 \times 10^{13} h^{-1} \text{ M}_\odot$  for superclusters selected with linking length  $L = 10, 7$ , and  $5 h^{-1} \text{ Mpc}$ , respectively. The maximum size of these superclusters ranges from  $\sim 150 h^{-1} \text{ Mpc}$  for  $L = 10 h^{-1} \text{ Mpc}$  to  $\sim 30 h^{-1} \text{ Mpc}$  for  $L = 5 h^{-1} \text{ Mpc}$ . The abundance of superclusters de-

creases rapidly with increasing redshift. There are many more superclusters at low  $z$  than at high  $z$  largely because there are many more clusters that have formed by the present time and that have gravitated to form superclusters. The richest superclusters are almost entirely missing at high redshifts; these structures form late in cosmic time. However, the densest “core” regions of superclusters, traced well by FOF linking lengths  $\sim 25\%$  of the mean intercluster separation, are present at  $z \approx 1$  almost as abundantly as they are today. These are likely the sites of the highest overdensities in the early Universe.

The spherically averaged density profiles of superclusters are well fit by an isothermal profile,  $n(r) \sim r^{-2}$ , over a broad range in radius. The profile is shallower at small radii and is steeper at large radii. A nearly linear relation exists between supercluster size and multiplicity, arising from this density profile.

The clusters residing in superclusters are more massive on average than un-clustered clusters, and clusters residing in rich superclusters are more massive than those in poorer superclusters.

We find that superclusters are triaxial in shape, especially at early times, where the mean triaxiality of our sample is  $T \approx 0.79$ . Over time, many collapse along a single dimension to approach two-dimensional shapes on the largest scales (i.e., those sampled by the FOF linking length  $L = 10h^{-1}$  Mpc at  $z \approx 0$ , using low-mass clusters with  $M_{vir} \geq 1.75 \times 10^{13}h^{-1}$  M<sub>⊙</sub>); their cores remain triaxial. Quantitatively, the mean triaxiality for long linking lengths decreases to  $T \approx 0.65$  at  $z \approx 0$ , whereas for smaller  $L$  (i.e., in the cores) it decreases to  $T \approx 0.69$ . The mean primary axis ratio of superclusters at  $z \approx 0$  is  $\sim 0.6$ , corresponding to a primary ellipticity  $\epsilon_1 \approx 0.4$ . Typical secondary axis ratios at  $z \approx 0$  are  $a_2/a_1 \approx 0.45$  ( $\epsilon_2 \approx 0.55$ ) for  $L = 5h^{-1}$  Mpc, and  $a_2/a_1 \approx 0.25$  ( $\epsilon_2 \approx 0.75$ ) for  $L = 10h^{-1}$  Mpc. Gravitational collapse increases ellipticity, as the potential gradient is larger along the minor rather than the major axis (Lin, Mestel, & Shu 1965); collapse thus leads to lower dimensionality (cf. Yoshisato et al. 2006, for a more recent treatment). A nonnegligible population of dense, filamentary superstructures is also present at  $z \approx 0$ , though not at higher redshift.

Superclusters selected using higher-mass clusters,  $M_{vir} \geq 10^{14}h^{-1}$  M<sub>⊙</sub>, show consistent results, with a reduced multiplicity function, as expected. These superclusters are triaxial in shape, with somewhat greater mean triaxiality at  $z \approx 0$  ( $T \approx 0.8$ -0.85) than superclusters with lower-mass clusters.

These properties, derived from a large-scale, high-resolution cosmological simulation, provide testable predictions of the currently favored  $\Lambda$ CDM model, with which future and currently accumulating observations can be compared. Once SDSS is complete, the best statistical analyses to date of large-scale structure using observations will be possible, especially

if accurate and well-behaved photo- $z$  algorithms are developed. There are other exciting observing programs on the horizon. The Pan-STARRS Project (Kaiser et al. 2002) is expected to see first light in 2006, and will carry out multi-band imaging surveys to identify galaxy clusters, as well as gravitational weak lensing observations to map the matter distribution in the Universe. The Large Synoptic Survey Telescope (Tyson 2002), which is expected to see first light in 2012, will provide improved weak lensing maps that will probe the dark matter distribution to the largest scales. The analysis presented here will aid in the comparison of these major observational data with the predictions of the concordance cosmological model.

This research was supported in part by NSF grant AST-0407305. Computations were performed on the National Science Foundation Terascale Computing System at the Pittsburgh Supercomputing Center; additional computational facilities at Princeton were provided by NSF grant AST-0216105.

## REFERENCES

Abell, G. O. 1958, *ApJS*, 3, 211

Bahcall, N. A. 1988, *ARA&A*, 26, 631

Bahcall, N. A. & Soneira, R. M. 1984, *ApJ*, 277, 27

Bahcall, N. A., Ostriker, J. P., Perlmutter, S., & Steinhardt, P. 1999, *Science*, 284, 1481

Bennett, C. L., et al. 2003, *ApJS*, 148, 1

Bode, P., & Ostriker, J. P. 2003, *ApJ*, 145, 1

Budavári, T., Szalay, A. S., Connolly, A. J., Csabai, I., & Dickinson, M. E. 2000, *AJ*, 120, 1588

Csabai, I., Connolly, A. J., Szalay, A. S., & Budavári, T. 2000, *AJ*, 119, 69

Davis, M., Efstathiou, G., Frenk, C. S., & White, S. D. M. 1985, *ApJ*, 292, 371

Einasto, M., Einasto, J., Tago, E., Dalton, G., & Andernach, H. 1994, *MNRAS*, 269, 301

Einasto, J., et al. 2003a, *A&A*, 405, 425

Einasto, J., et al. 2003b, *A&A*, 410, 425

Geller, M. J., & Huchra, J. P. 1989, *Science*, 246, 897

Gott, J. R., et al. 2003, *astro-ph/0310571*

Gregory, S. A., & Thompson, L. A. 1978, *ApJ*, 222, 784

Gregory, S. A., Thompson, L. A., & Tifft, W. G. 1981, *ApJ*, 243, 411

Hopkins, P. F., Bahcall, N., & Bode, P. 2005, *ApJ*, 618, 1

Hubble, E. 1936, *The Realm of the Nebulae* (New Haven: Yale University Press)

Kaiser, N., et al. 2002, *Proc. SPIE*, 4836, 154

Kolokotronis, V., Basilakos, S., & Plionis, M. 2002, *MNRAS*, 331, 1020

Lin, C. C., Mestel, L., & Shu, F. H. 1965, *ApJ*, 142, 1431

Navarro, J. F., Frenk, C. S., & White, S. D. 1996, *ApJ*, 462, 563

Navarro, J. F., Frenk, C. S., & White, S. D. 1997, *ApJ*, 490, 493

Oort, J. H. 1983, *ARA&A*, 21, 373

Ostriker, J. P., & Steinhardt, P. J. 1995, *Nature*, 377, 600

Peacock, J. A. 1999, *Cosmological Physics* (Cambridge, UK: University Press)

Spergel, D. N., et al. 2003, *ApJS*, 148, 175

Statler, T. S. 1994, *AJ*, 108, 111

Stoughton, C., et al. 2002, *AJ*, 124, 1810

Tyson, J. A. 2002, *Proc. SPIE*, 4836, 10

York, D. G., et al. 2000, *AJ*, 120, 1579

Yoshisato, A., Morikawa, M., Gouda, N., & Mouri, H. 2006, *ApJ*, 637, 555

Table 1: Supercluster Axis Ratios at  $z \approx 0$

$L$	Mean $a_2/a_1$	Peak $a_2/a_1$	Mean $a_3/a_2$	Peak $a_3/a_2$
5	$0.60 \pm .009$	0.64	$0.50 \pm .007$	0.41
7	$0.57 \pm .004$	0.62	$0.43 \pm .003$	0.31
10	$0.54 \pm .002$	0.64	$0.33 \pm .001$	0.20

Note. — Peaks and mean values of the distributions shown in Figs. 7-8. Statistical errors are given for the mean values.

Table 2: Evolution of the Primary Axis Ratio  $a_2/a_1$

$z$	$b = 0.23$	$b = 0.33$	$b = 0.47$
0	$0.60 \pm .009$	$0.57 \pm .004$	$0.54 \pm .002$
1	$0.44 \pm .03$	$0.47 \pm .01$	$0.48 \pm .01$
2	$0.52 \pm .06$	$0.50 \pm .03$	$0.50 \pm .02$

Note. — Mean values are given as a function of the linking length parameter  $b$ . Statistical errors are given. Note that  $b = 0.23$  corresponds to  $L_{z=0} = 5h^{-1}$  Mpc,  $b = 0.33$  to  $L_0 = 7h^{-1}$  Mpc, and  $b = 0.47$  to  $L_0 = 10h^{-1}$  Mpc.

Table 3: Evolution of the Secondary Axis Ratio  $a_3/a_2$

$z$	$b = 0.23$	$b = 0.33$	$b = 0.47$
0	$0.50 \pm .007$	$0.43 \pm .003$	$0.33 \pm .001$
1	$0.36 \pm .02$	$0.40 \pm .01$	$0.44 \pm .01$
2	$0.41 \pm .05$	$0.41 \pm .03$	$0.46 \pm .01$

Note. — Mean values are given as a function of the linking length parameter  $b$ . Statistical errors are given.

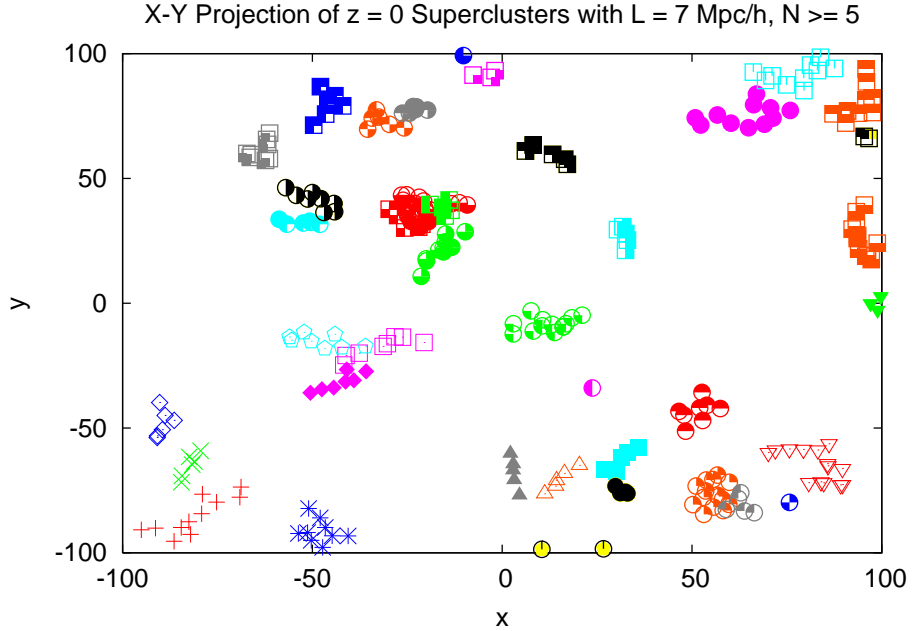


Fig. 1.— Clusters identified as supercluster members at redshift zero, for  $L = 7 \text{ Mpc}/h$  and minimum multiplicity 5. Clusters represented by similar points are members of the same supercluster. See the text (§2.3) for further description.

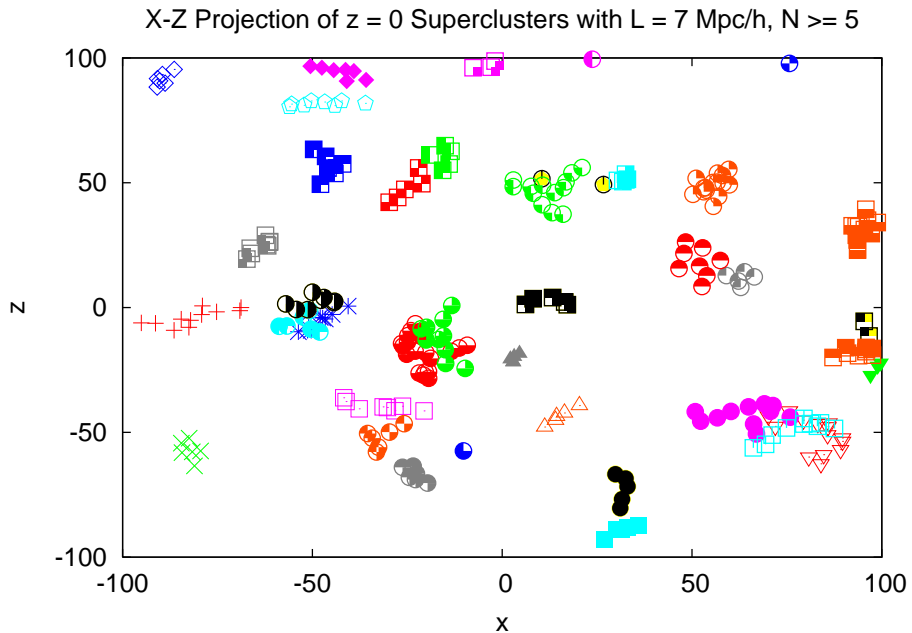


Fig. 2.— Same parameters as Fig. 1, but a different projection.

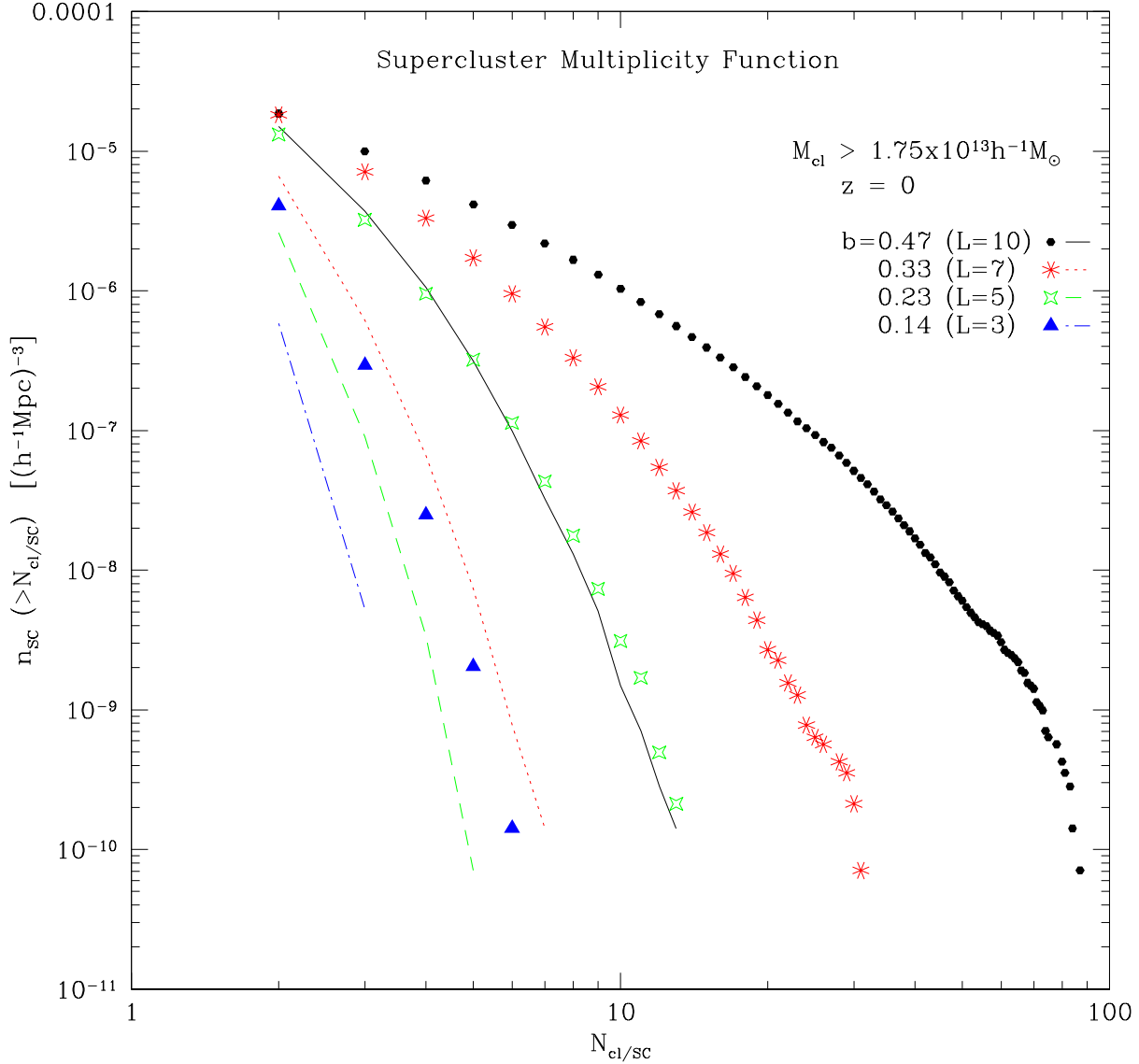


Fig. 3.— Integrated supercluster multiplicity functions for linking lengths  $L = 3, 5, 7$ , and  $10 h^{-1} \text{Mpc}$ , all at  $z \approx 0$ . Curves show superclusters identified in our random Monte Carlo simulations to test the physical reality of the superclusters.

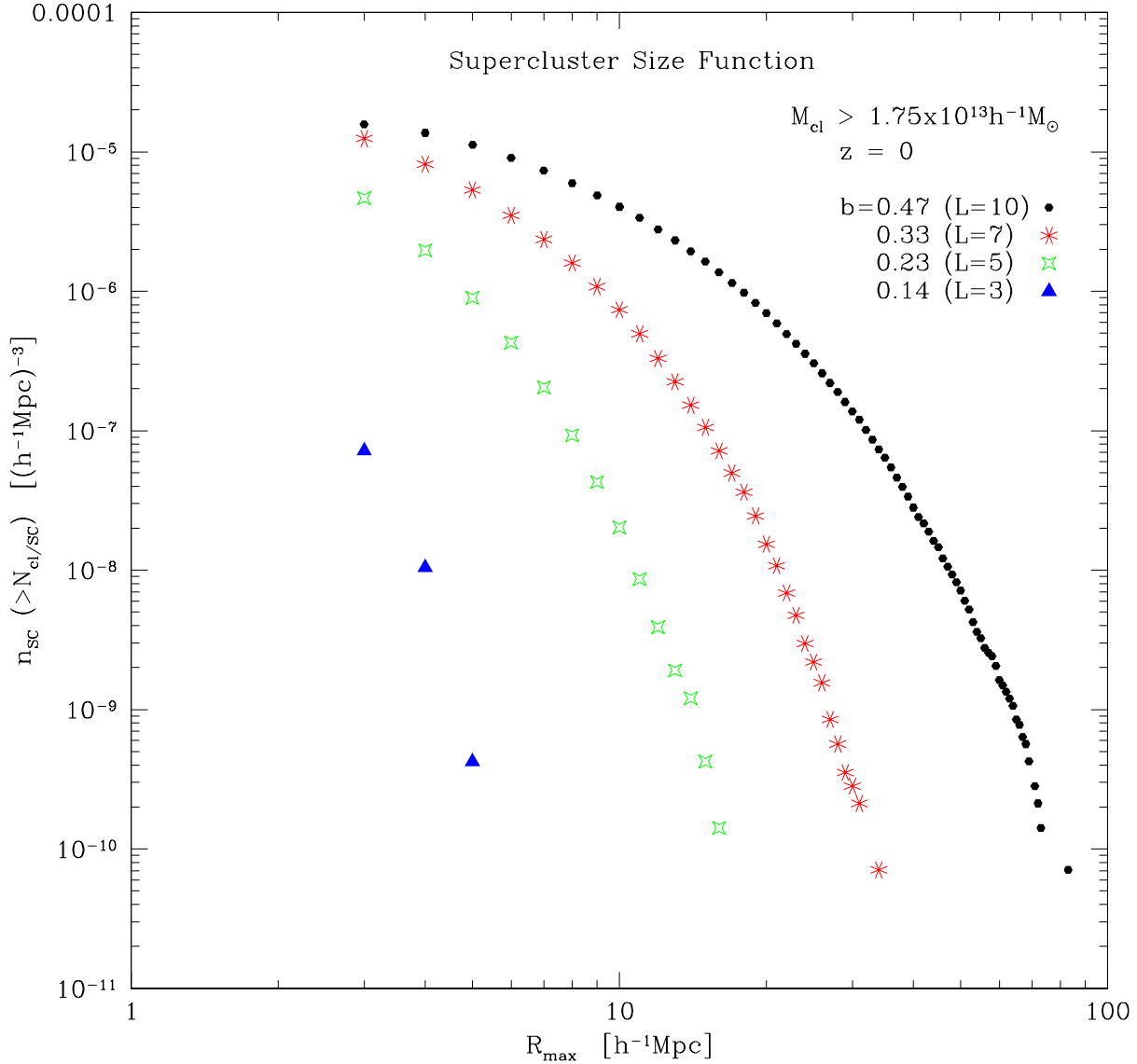


Fig. 4.— Integrated size functions for linking lengths  $L = 3, 5, 7$ , and  $10 h^{-1} \text{Mpc}$  at  $z \approx 0$ . The size measurement along the horizontal axis is, for a given supercluster, the distance of the member cluster most distant from the supercluster center of mass. All are comoving scales.

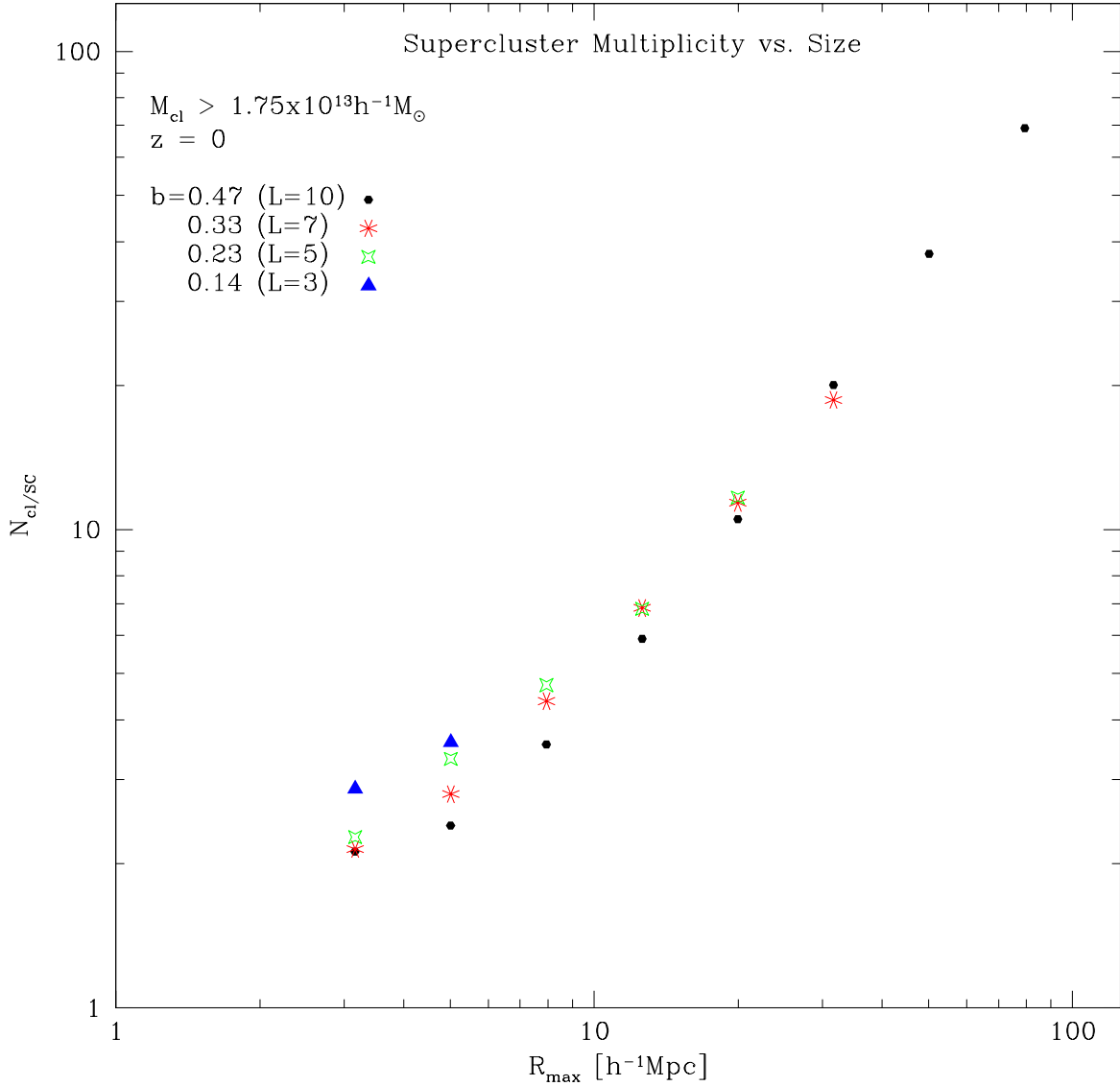


Fig. 5.— Multiplicity vs. size of superclusters,  $z \approx 0$ .  $R_{\text{max}}$  is defined as in Fig. 4. Linking lengths  $L$  are quoted in  $h^{-1} \text{Mpc}$ .

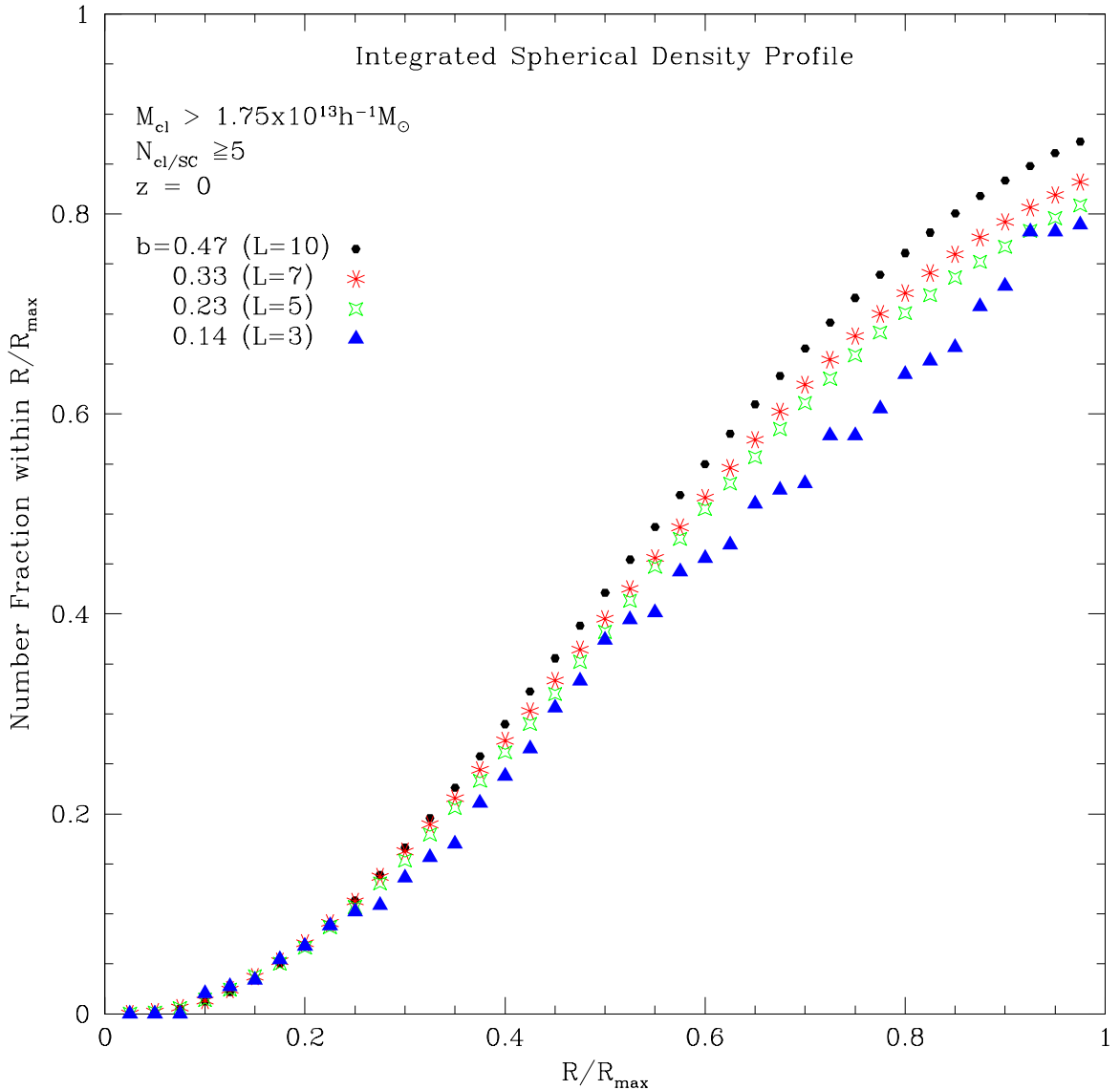


Fig. 6.— Integrated number fraction of clusters in superclusters of minimum multiplicity 5, at  $z \approx 0$ . Linking lengths  $L$  are quoted in  $h^{-1} \text{Mpc}$ .

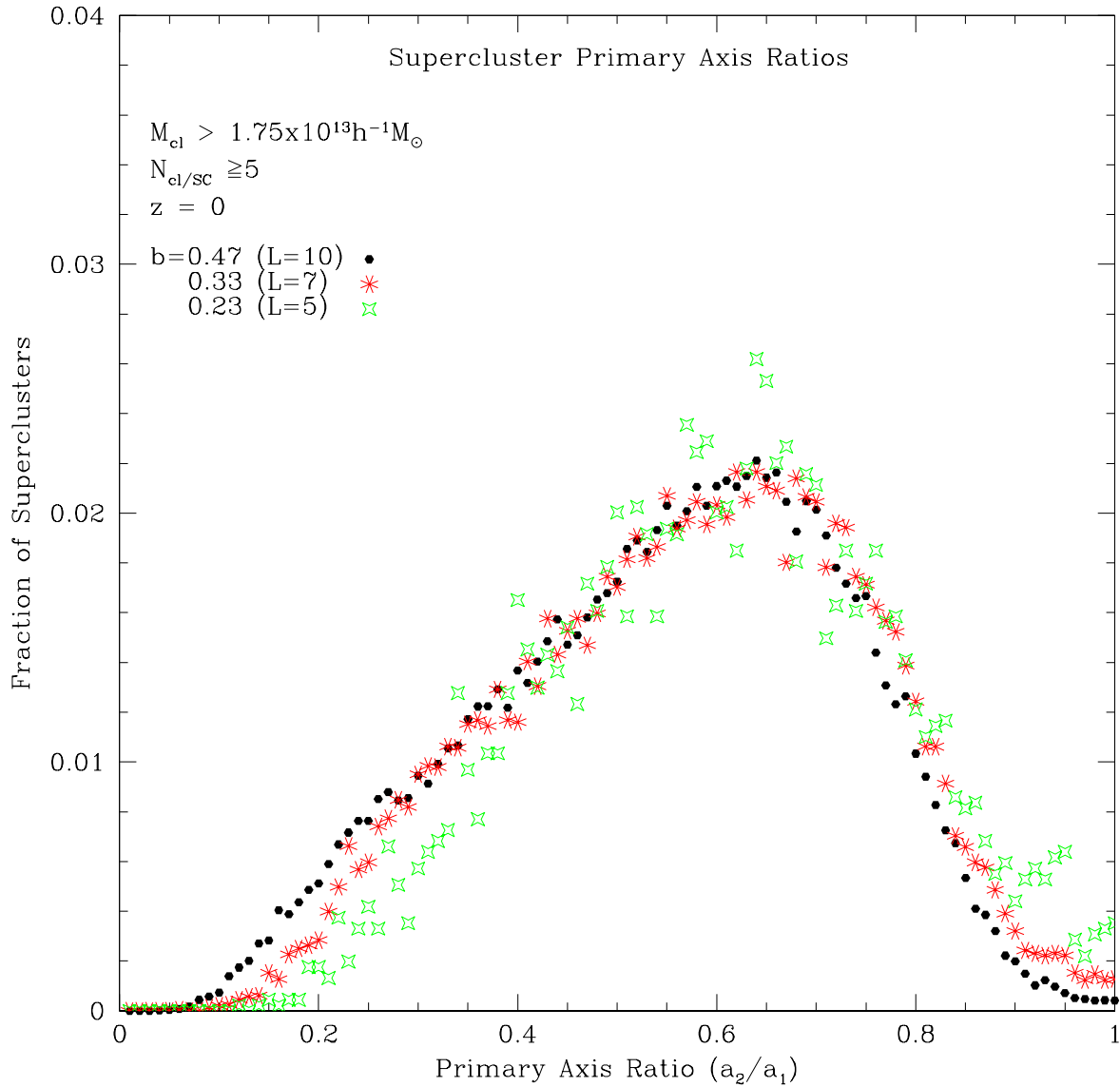


Fig. 7.— Distributions of supercluster primary axis ratios for various linking lengths, at  $z \approx 0$ . The scale along the vertical axis is arbitrary. Linking lengths  $L$  are quoted in  $h^{-1} \text{ Mpc}$ .

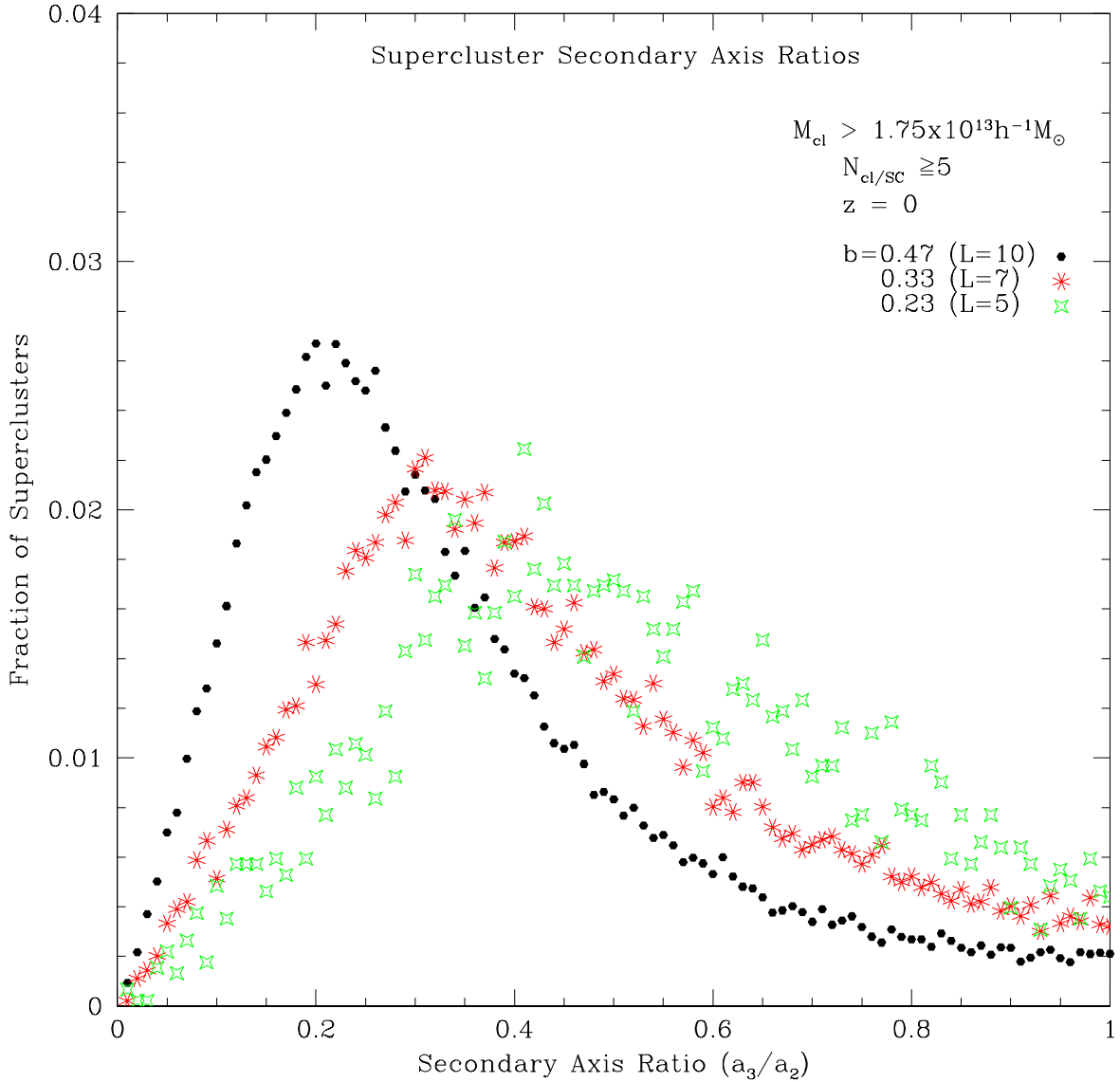


Fig. 8.— Distributions of supercluster secondary axis ratios for various linking lengths, at  $z \approx 0$ . As in Fig. 7, the scale along the vertical axis is arbitrary. Linking lengths  $L$  are quoted in  $h^{-1}$  Mpc.

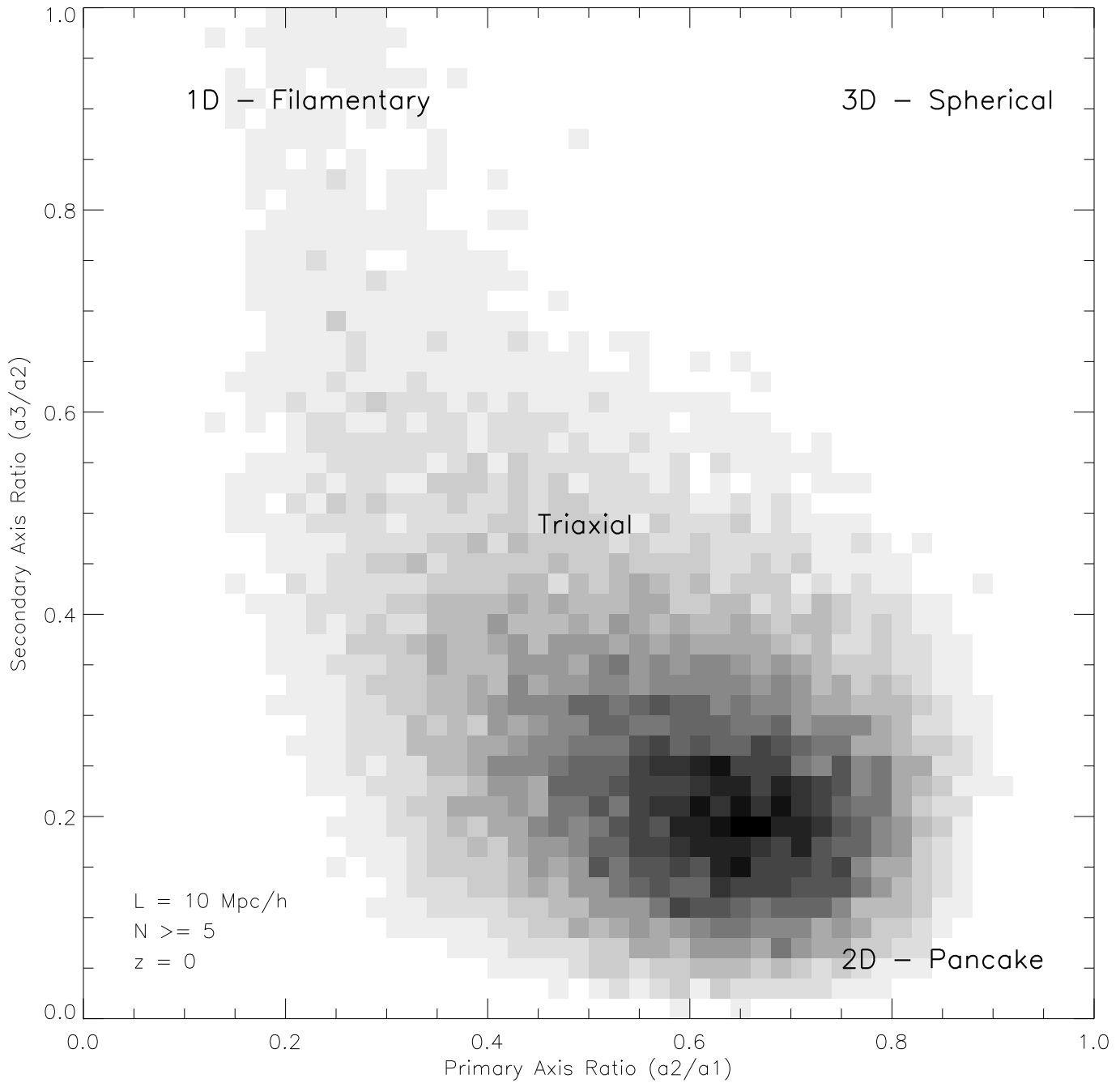


Fig. 9.— Bivariate distribution of primary and secondary axis ratios for low- $z$  superclusters found with linking length  $L = 10h^{-1}$  Mpc. See the text (§6) for interpretation.

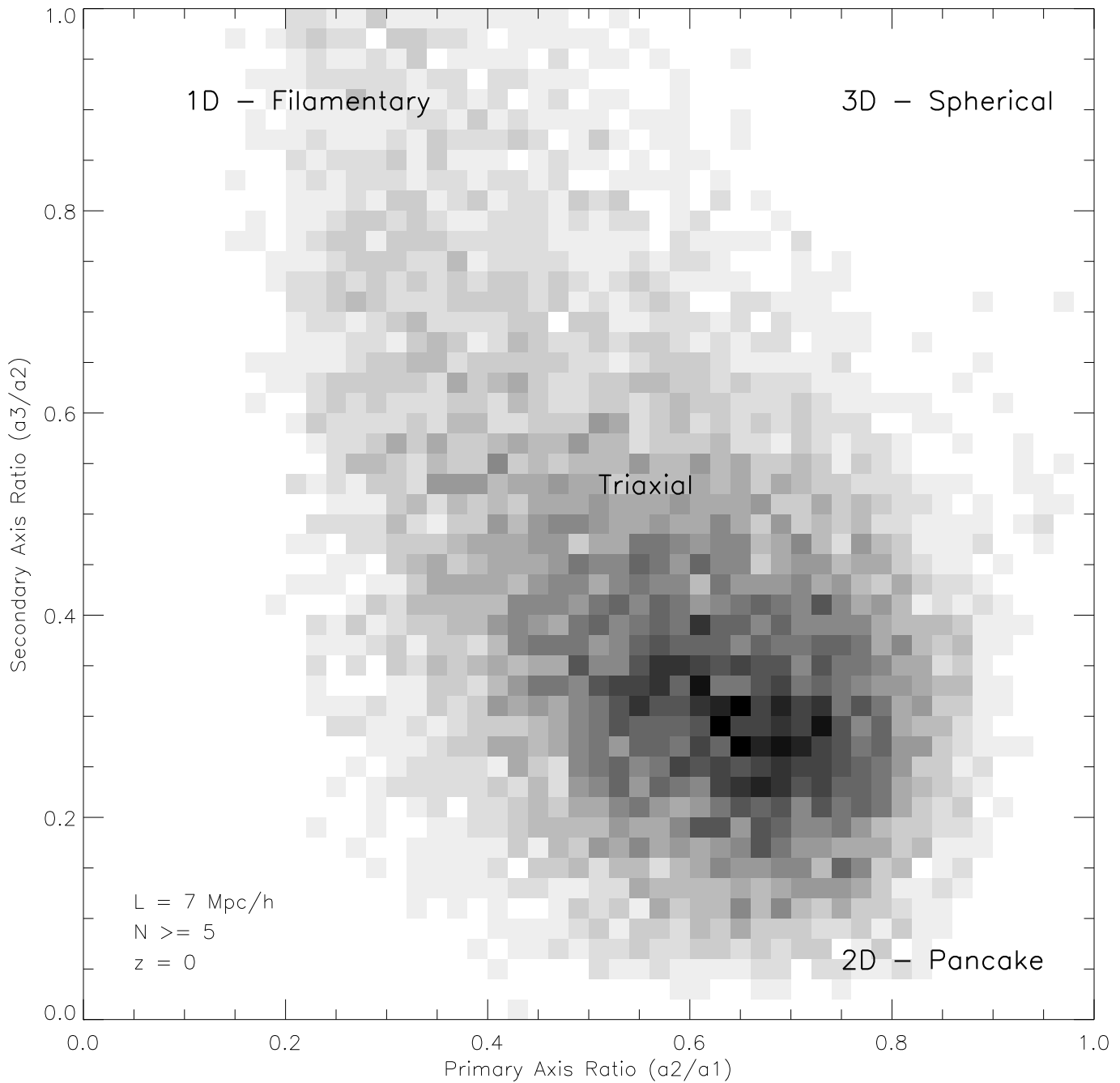


Fig. 10.— Same as Fig. 9, but for low- $z$  superclusters found with  $L = 7h^{-1} \text{ Mpc}$ .

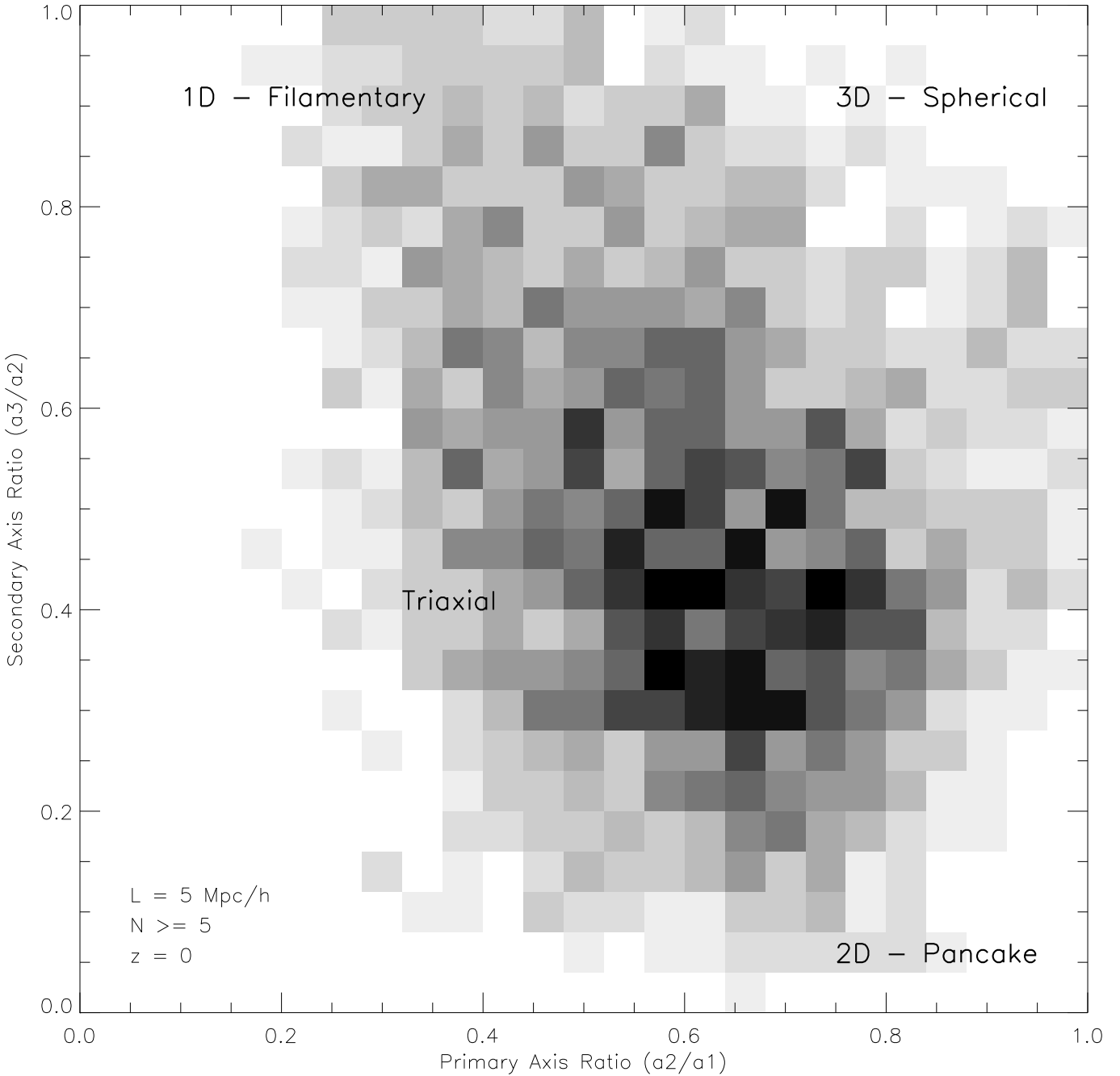


Fig. 11.— Same as Fig. 9, but for low- $z$  superclusters found with  $L = 5h^{-1} \text{ Mpc}$ . Larger bins are used in this plot because there are few superclusters with  $N \geq 5$  for this  $L$ -value.

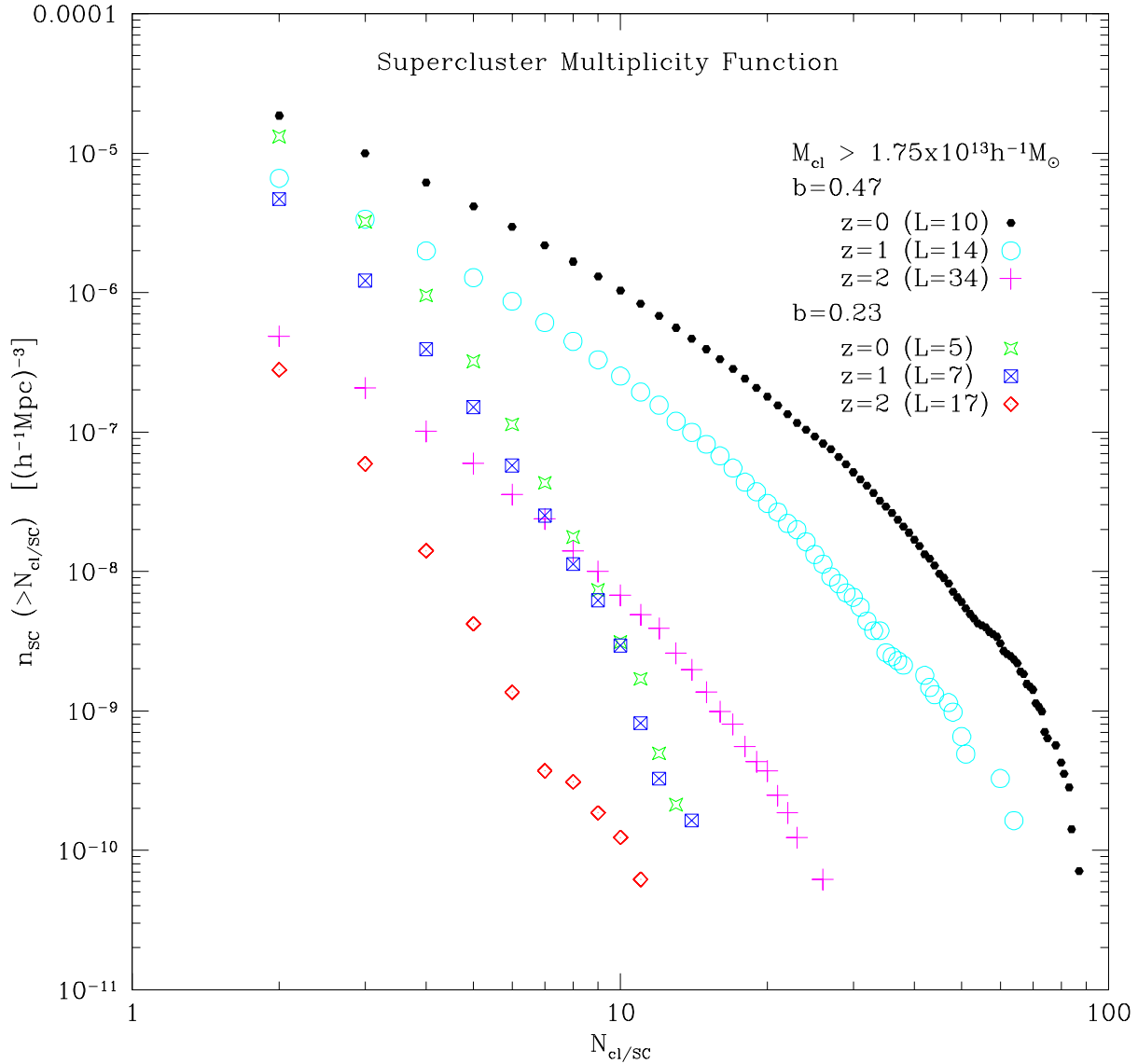


Fig. 12.— Evolution of the integrated supercluster multiplicity function with redshift. Linking lengths  $L$  are quoted in  $h^{-1} \text{Mpc}$ .

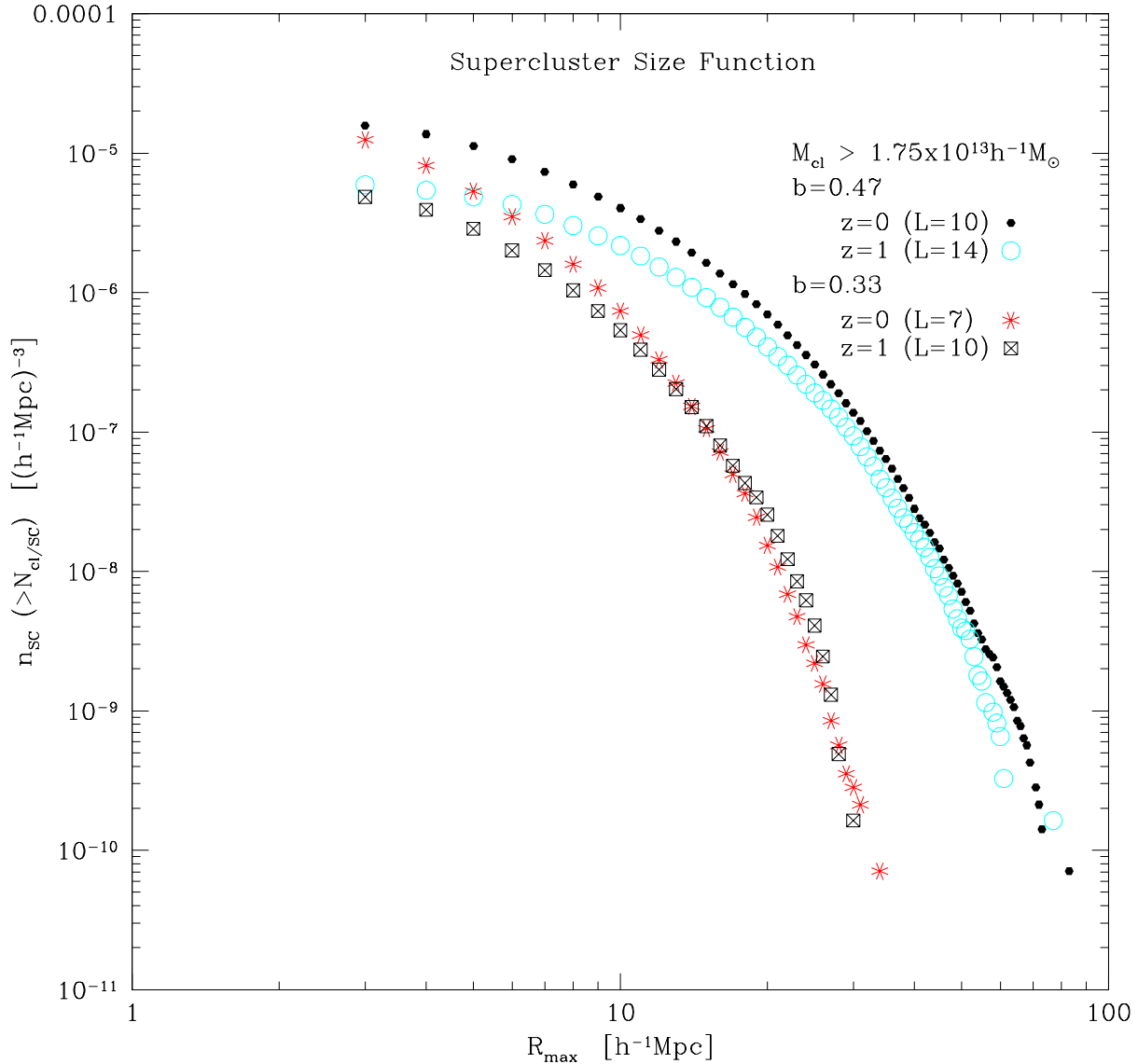


Fig. 13.— Evolution of the integrated supercluster size function (comoving scales) with redshift. Linking lengths  $L$  are quoted in  $h^{-1}$  Mpc.

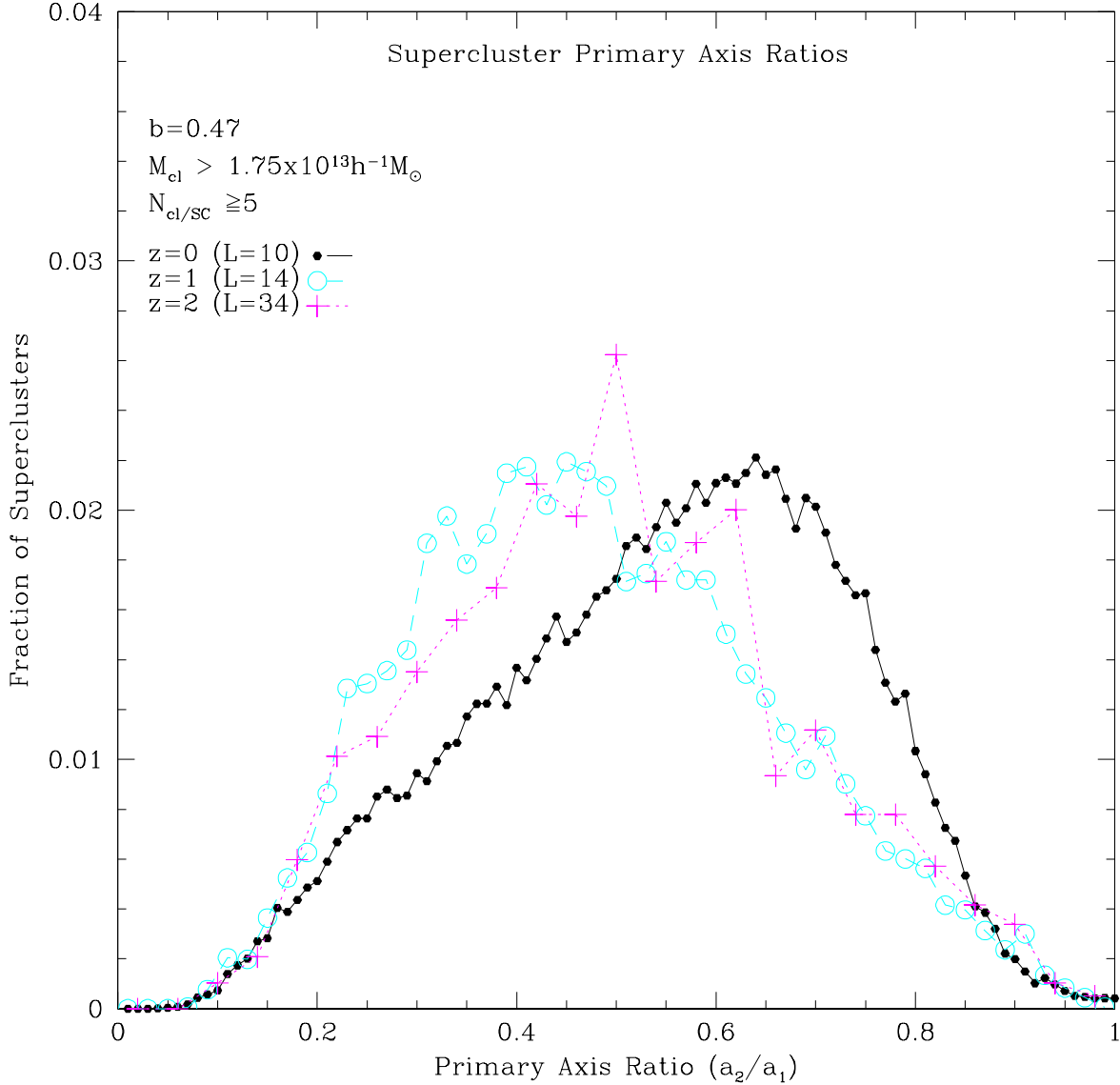


Fig. 14.— Evolution of supercluster primary axis ratios with redshift. All curves are generated from superclusters selected with linking length parameter  $b = 0.47$ . The points are connected for clarity. Linking lengths  $L$  are quoted in  $h^{-1}$  Mpc.

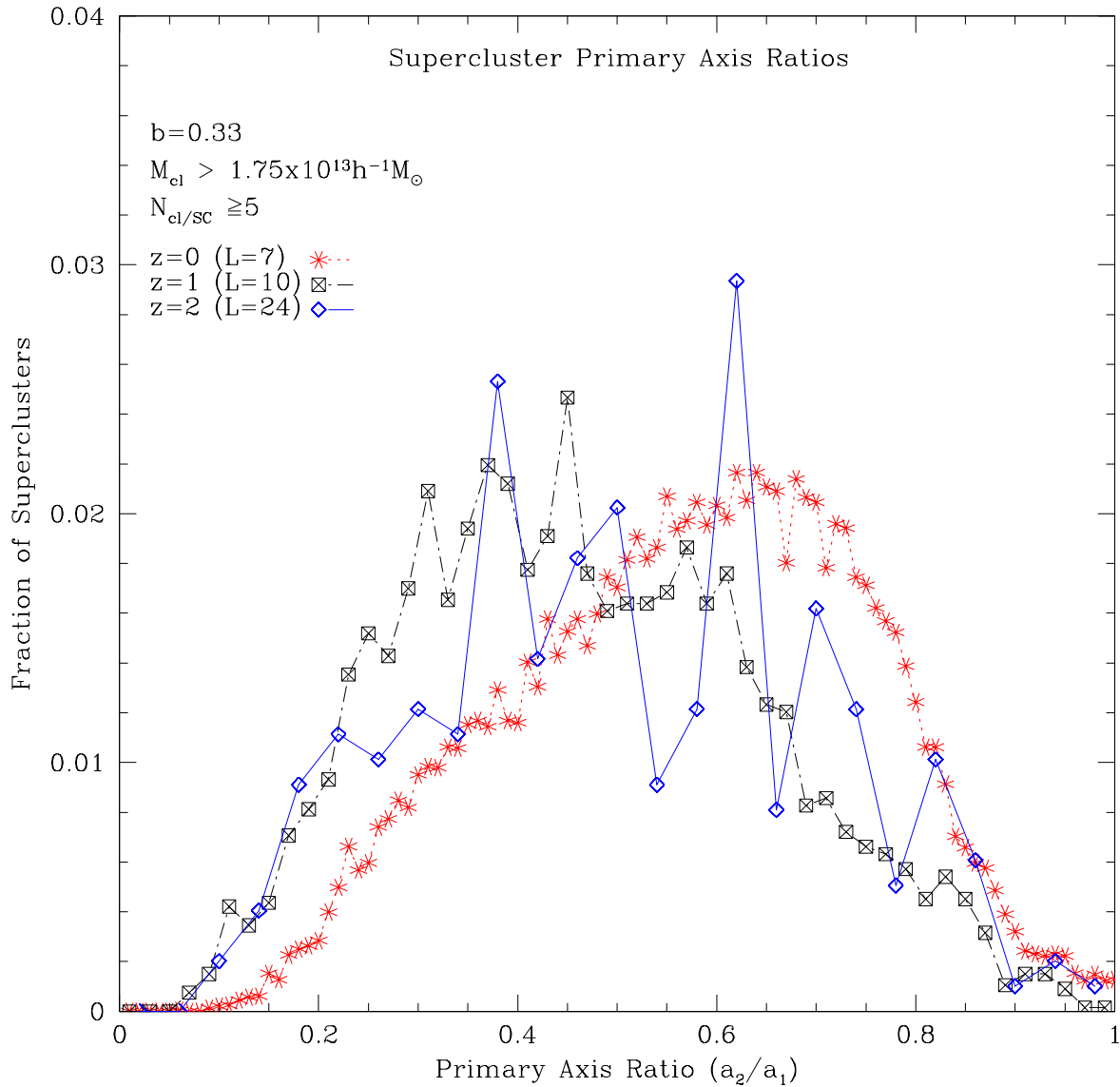


Fig. 15.— Same as Fig. 14, but for the linking length parameter  $b = 0.33$ .

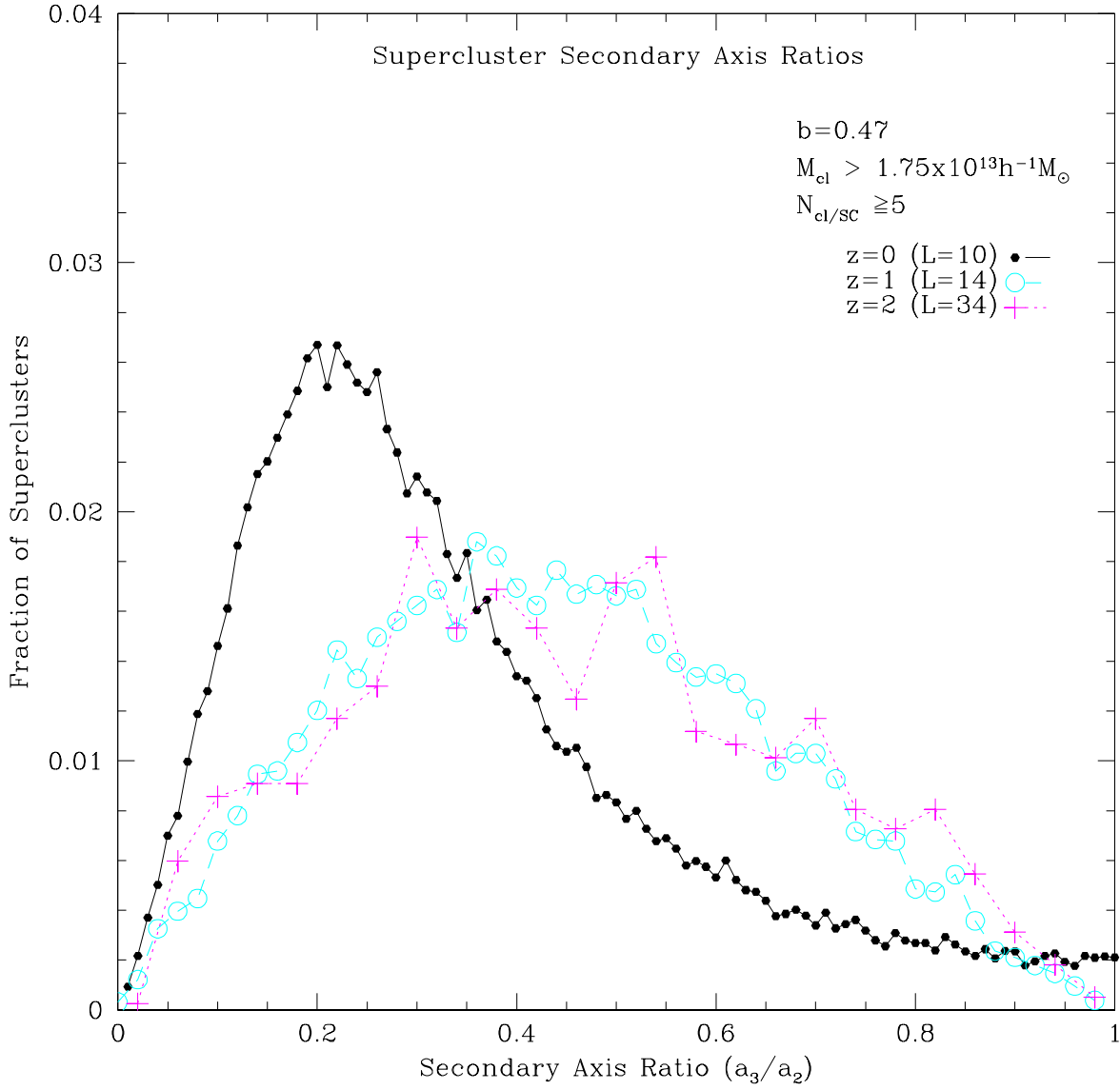


Fig. 16.— Evolution of supercluster secondary axis ratios with redshift. All curves are generated from superclusters selected with linking length parameter  $b = 0.47$ . Linking lengths  $L$  are quoted in  $h^{-1}$  Mpc.

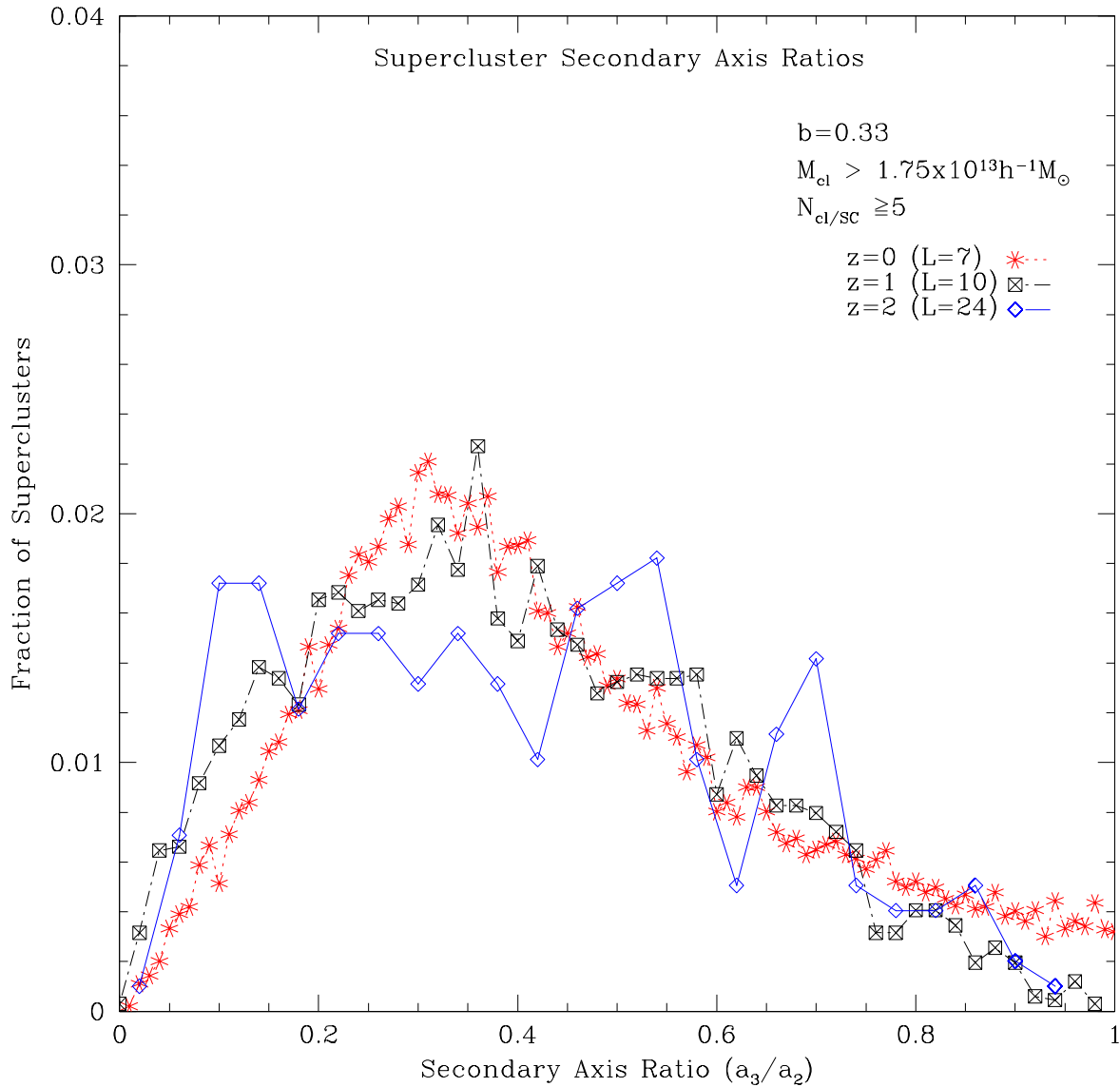


Fig. 17.— Same as Fig. 16, but for the linking length parameter  $b = 0.33$ .

X-Y Projection of  $z = 0$  Superclusters with  $b = 0.33$ ,  $N \geq 3$  (Hi-Mass Clusters Only)

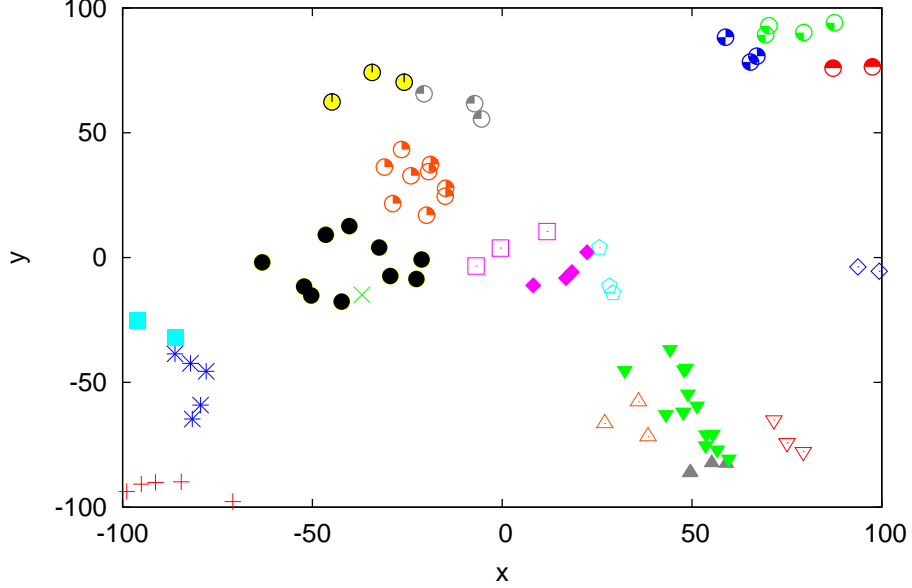


Fig. 18.— Superclusters selected using high-mass clusters ( $M_{vir} \geq 10^{14}h^{-1} M_{\odot}$ ) at redshift zero, for  $b = 0.33$  and multiplicity  $\geq 5$ . Clusters represented by similar points are members of the same supercluster.

X-Z Projection of  $z = 0$  Superclusters with  $b = 0.33$ ,  $N \geq 3$  (Hi-Mass Clusters Only)

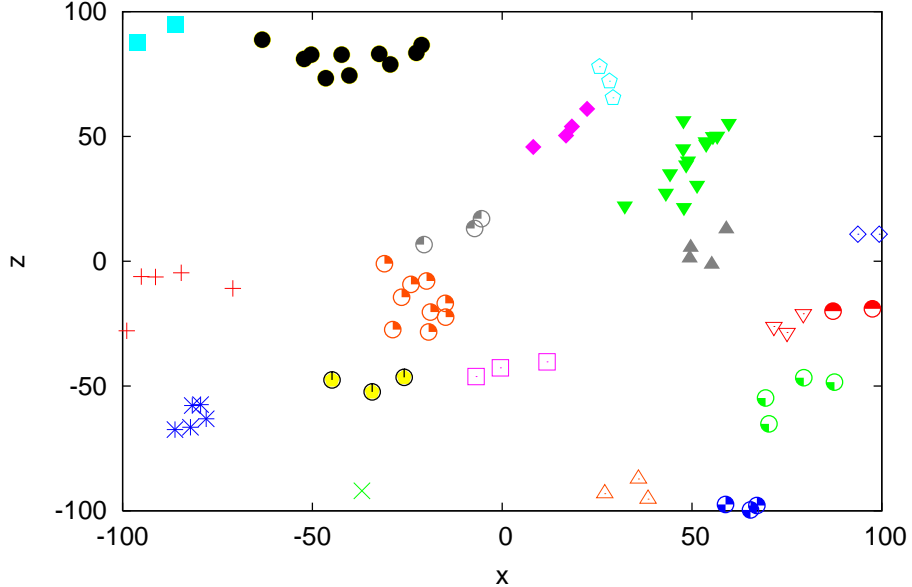


Fig. 19.— Same as Fig. 18, but a different projection.

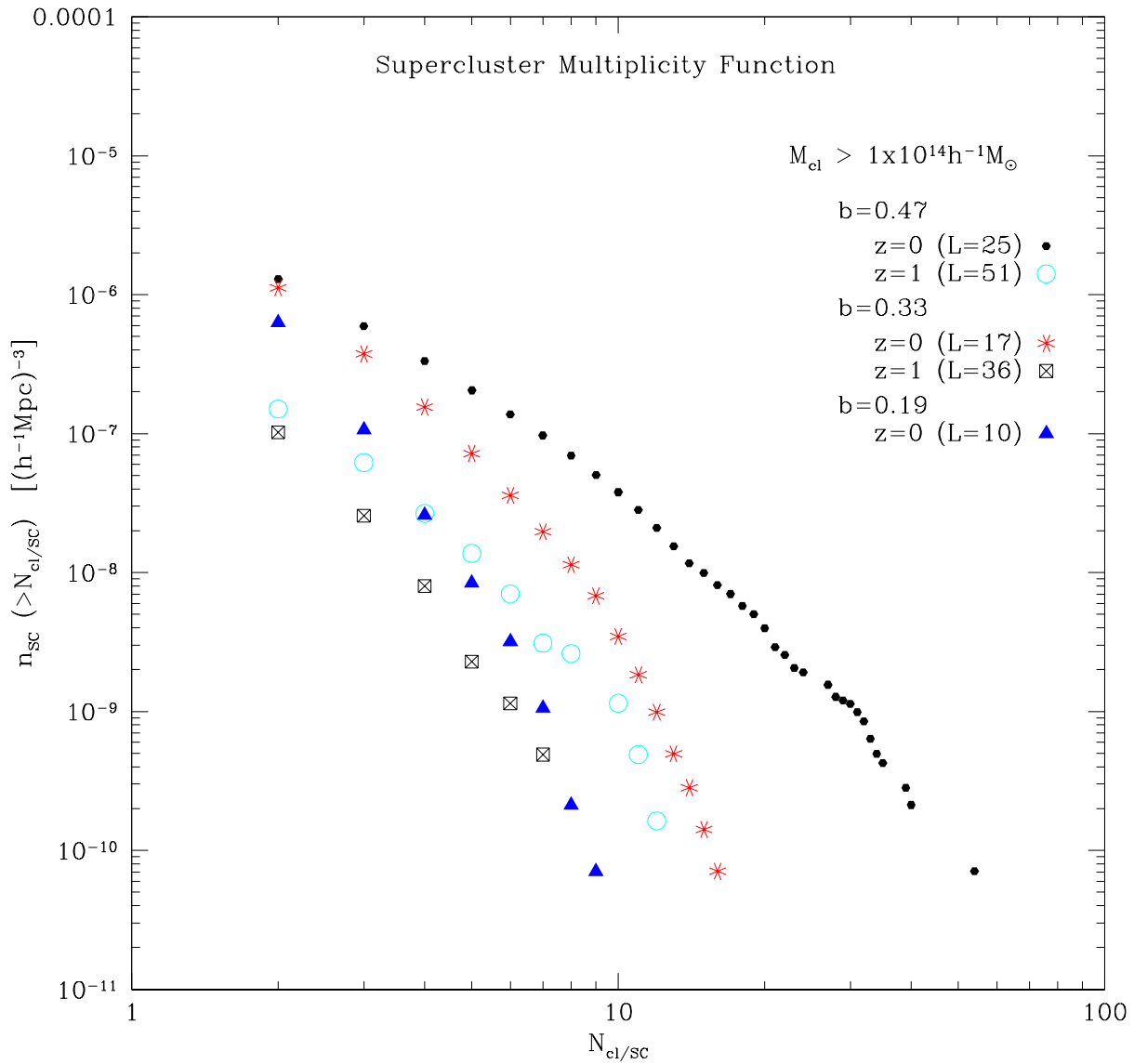


Fig. 20.— Integrated supercluster multiplicity functions for superclusters selected using only high-mass clusters,  $M_{\text{vir}} \geq 10^{14} h^{-1} M_{\odot}$ . Linking lengths  $L$  are quoted in  $h^{-1} \text{Mpc}$ .

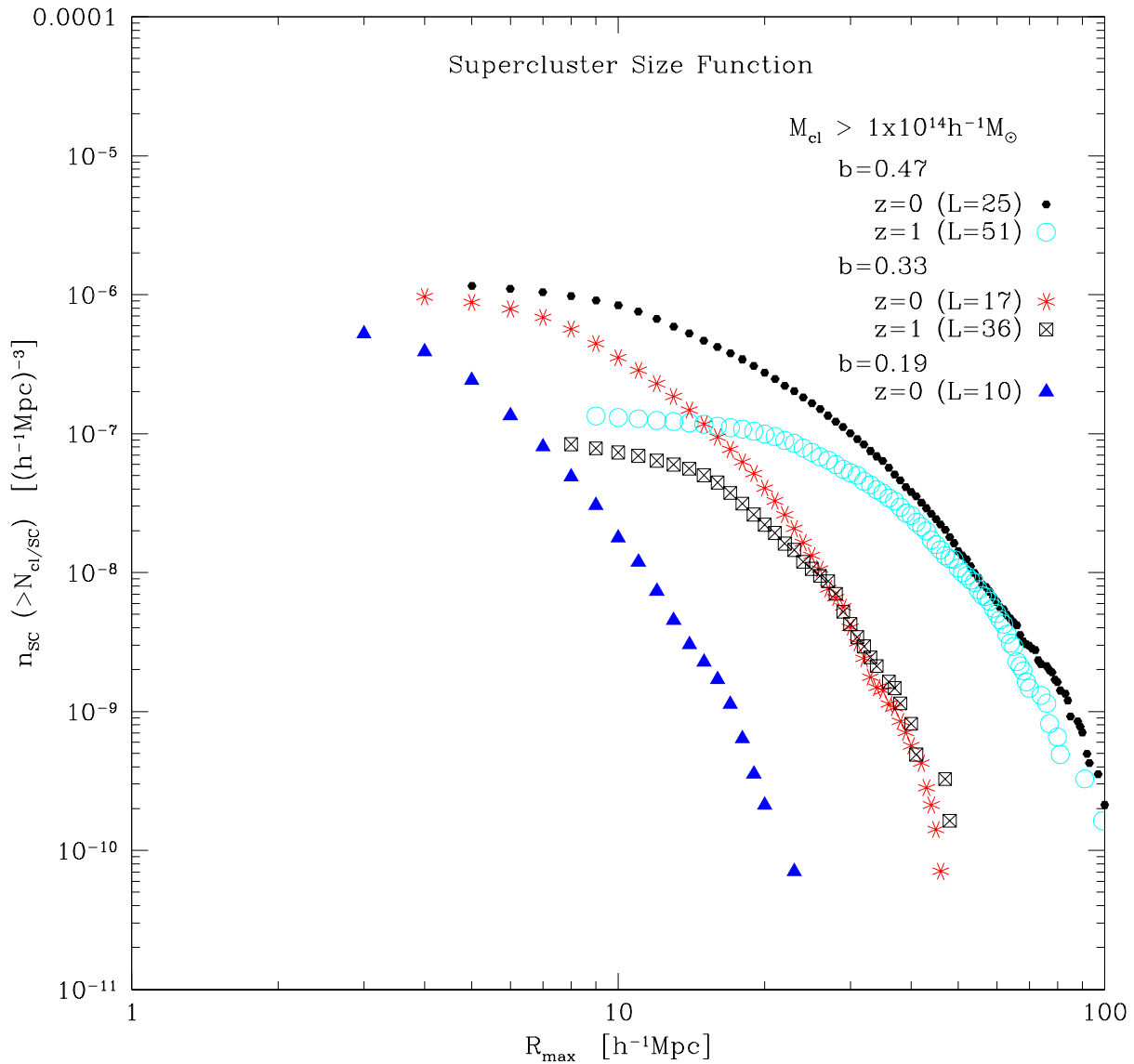


Fig. 21.— Integrated supercluster size functions for superclusters selected using only high-mass clusters,  $M_{\text{vir}} \geq 10^{14} h^{-1} M_{\odot}$ . Linking lengths  $L$  are quoted in  $h^{-1} \text{Mpc}$ .

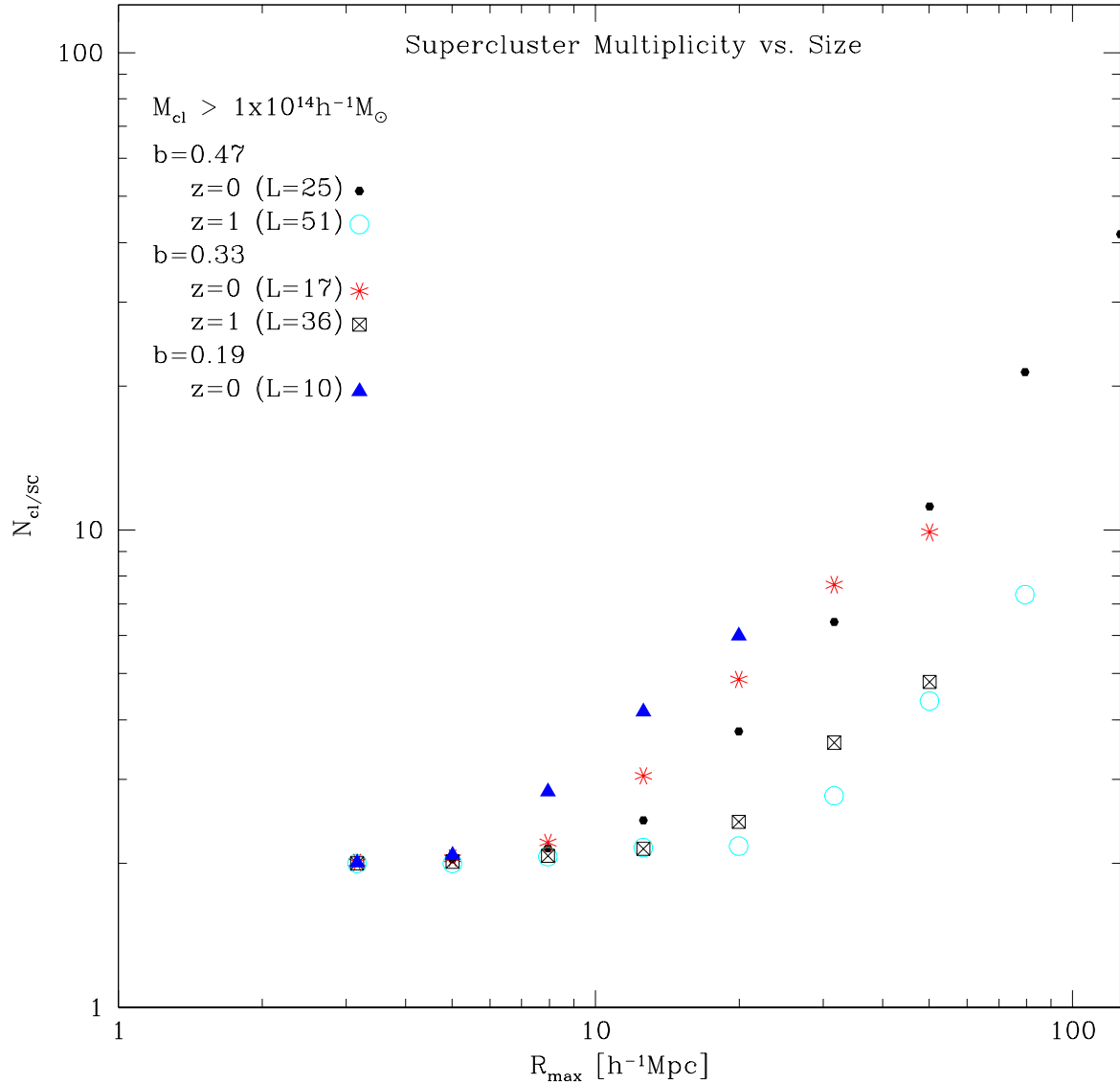


Fig. 22.— Multiplicity vs. size of superclusters selected using only high-mass clusters,  $M_{\text{vir}} \geq 10^{14} h^{-1} M_{\odot}$ . Linking lengths  $L$  are quoted in  $h^{-1} \text{Mpc}$ .

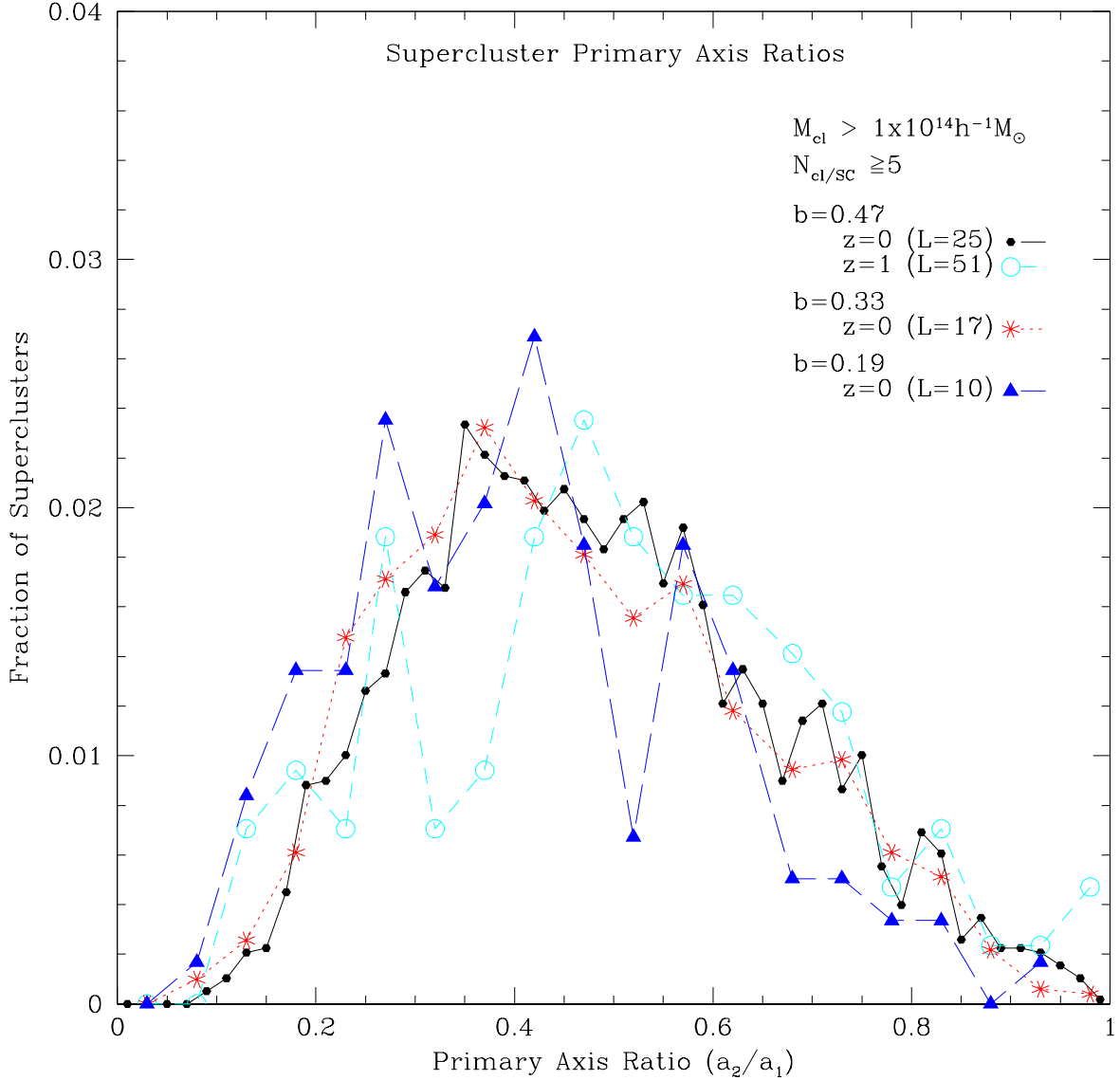


Fig. 23.— Distributions of supercluster primary axis ratios for superclusters selected using only high-mass clusters,  $M_{\text{vir}} \geq 10^{14} h^{-1} M_{\odot}$ . Linking lengths  $L$  are quoted in  $h^{-1}$  Mpc.

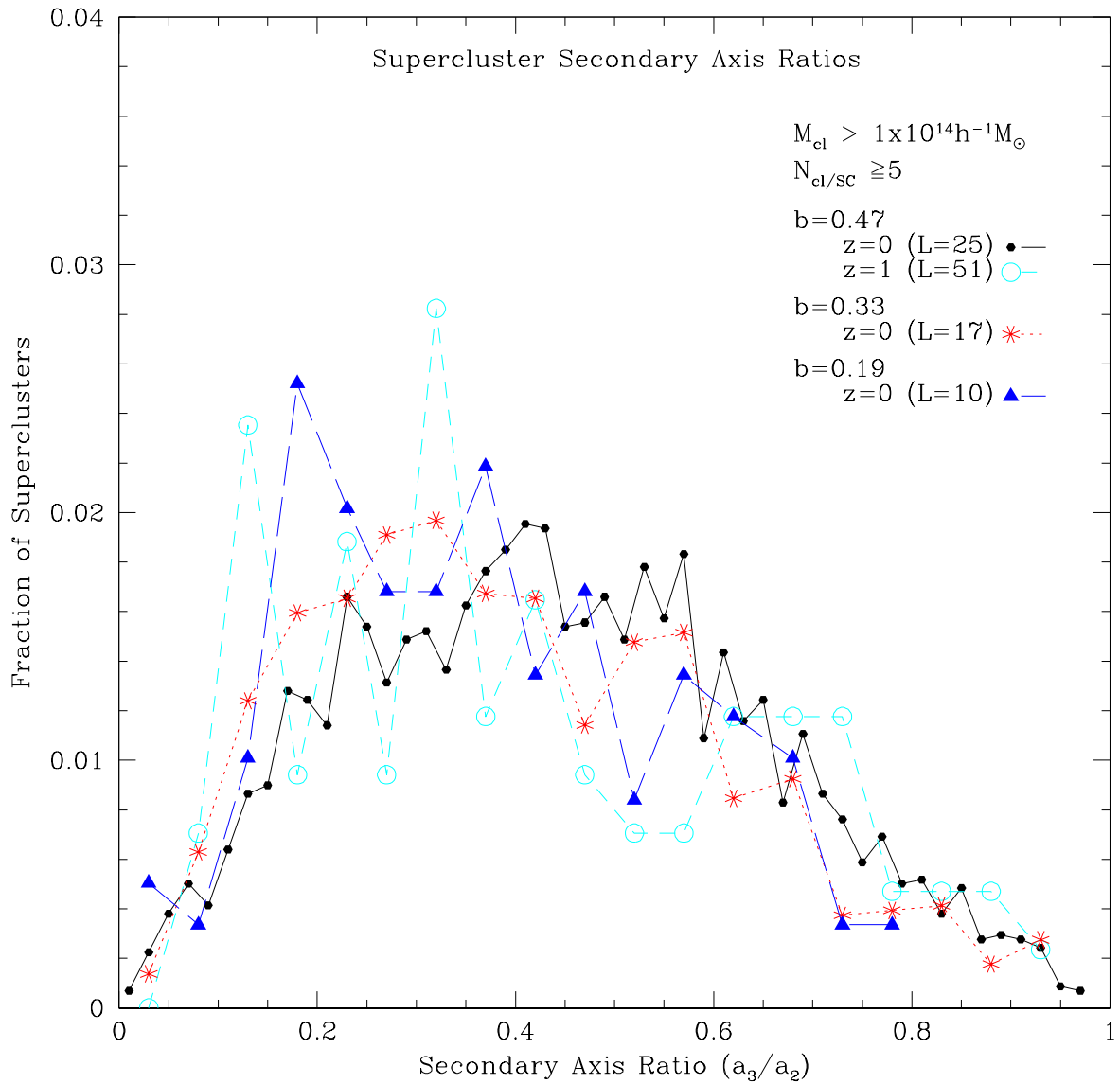


Fig. 24.— Distributions of supercluster secondary axis ratios for superclusters selected using only high-mass clusters,  $M_{\text{vir}} \geq 10^{14} h^{-1} M_{\odot}$ . Linking lengths  $L$  are quoted in  $h^{-1} \text{Mpc}$ .